https://doi.org/10.5194/ar-2026-2
Preprint. Discussion started: 3 February 2026

AEROSOL Research Discussions

From seeding to detachment: leveraging deep learning to quantify the transport of tire wear microplastics in a wind tunnel

Bashir Olasunkanmi Ayinde[1], Wolfgang Babel[1,2], Johannes Olesch[1,2], Daniel Wagner[3], Seema Agarwal[3], Christian Laforsch[4], Julian Brehm[4], Anke Nölscher[5,*], and Christoph Karl Thomas[1,2]

[1]Micrometeorology Group, University of Bayreuth, Germany
[2]Bayreuth Center for Ecology and Environmental Research, University of Bayreuth, Germany
[3]Department of Macromolecular Chemistry II, University of Bayreuth, Germany
[4]Chair of Animal Ecology I, University of Bayreuth, Germany
[5]Atmospheric Chemistry, Bayreuth Center of Ecology and Environmental Research (BayCEER), University of Bayreuth, Bayreuth, Germany
[*]*now at: Institute of Climate and Energy Systems, ICE-3: Troposphere, Forschungszentrum Jülich GmbH, Jülich, Germany, and Institute of Geophysics and Meteorology, University of Cologne, Cologne, Germany

Correspondence: Bashir Olasunkanmi Ayinde (Bashir.Ayinde@uni-bayreuth.de)

Abstract. The transport dynamics of tire wear particles (TWPs) remain poorly understood despite their growing contribution to airborne microplastic (MP) pollution. This study addresses this gap by experimentally quantifying the TWP detachment rate and threshold friction velocities (u_*^{th}) from an idealised reference surface. Detachment experiments were conducted in a boundary layer wind tunnel over glass substrates seeded with a near-monolayer of particles. Time resolved imaging at 0.1 Hz was combined with automatic particle detachment and segmentation using an open source You Only Look Once version 8 nano (YoloV8n) model, which allowed individual detachment events and particle size and shape to be tracked with a mean average precision at an intersection-over-union threshold of 0.5 (mAP@50) above 85 % for both the bounding box and mask outputs. For the detachment experiments, pristine tire wear particles generated on a laboratory test stand with passenger car (PC) test tire were supplied by Continental GmbH, providing a well characterised and idealised TWP source. Among the three deposition method tested, the low-cost pressurised seeding approach produced the most uniform and reproducible particle distribution for detachment analysis. Across the analysed size range (80 to 300 μm), larger and more irregularly shaped particles exhibited significantly higher detachment (u_*^{th}) than smaller and more rounded fragments. Ensemble fits yield a bulk u_*^{th} of approximately 0.36 m s^{-1}, with size and shape resolved u_*^{th} values varying by roughly a factor of 1.5 between the most easily detached and most resistant classes. The application of the Shao and Lu semi-empirical fluid threshold model reproduced the size-dependent u_*^{th} of smooth PE microsphere, but underestimates the TWP u_*^{th} unless the effective cohesion and/or aerodynamic scaling parameter are increased beyond values typically used for dust and sand. This behaviour is consistent with TWPs experiencing stronger effective adhesion than smooth, spherical grains of similar size, due to their irregular morphology and multiple contact points with the substrate. The density differences between TWPs (~ 1300 kg m^{-3}) and microspheres (~ 1025 kg m^{-3}) showed negligible influence within the studied size range (106 to 125 μm). We conclude that particle morphology, incorporating both size and shape, plays a dominant role in controlling the aerodynamic detachment of TWPs on the idealised glass substrate, while density effects are secondary under the tested conditions. Because controlled laboratory studies using well defined particles

https://doi.org/10.5194/ar-2026-2
Preprint. Discussion started: 3 February 2026

and simplified surfaces are a neccessary step towards isolating these fundamental mechanisms, our findings provide insights for improving MP and TWP resuspension models and highlight the need for future studies on more realistic environmental surfaces and broader particle sizes and density ranges.

Graphical Abstract

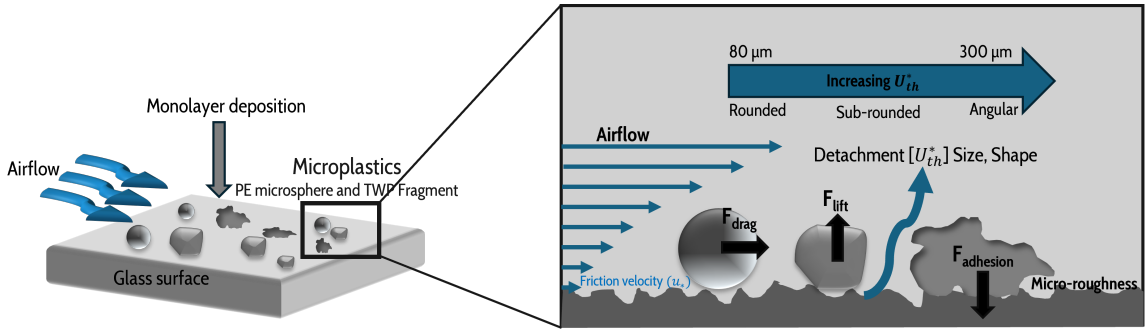

1 Introduction

Microplastics (MPs) defined as plastic particles smaller than 5 mm are among the highly discussed topics that have garnered significant global attention due to their ubiquitous nature in the environment (Arthur et al., 2009; Sundt et al., 2014). Although tire wear particles (TWPs) have been recognised as pollutants since the late 1970s (Cadle and Williams, 1978), they were only recently identified as MPs (Sundt et al., 2014). Earlier studies on MPs primarily focused on microbeads from pharmaceuticals and personal care products (Gregory, 1996), as well as fragmentation and weathering of larger plastics. These particles find their way into all environmental compartments, having multifaceted impacts on the ecosystems, organisms, and human health (Luo et al., 2021; Osuoha et al., 2023; Piehl et al., 2018; Horton and Dixon, 2018; Laforsch et al., 2021). In recent years, more attention has been given to MPs in marine environments and their shorelines (Laglbauer et al., 2014; van Calcar and van Emmerik, 2019). However, as more research emerges on this interest, we see the need to investigate MP transports in other environmental compartments, including the terrestrial ecosystem, urban air and non-exhaust traffic particles, thereby drawing more attention to additional, less obvious MP sources and materials, including TWPs (Laermanns et al., 2021; Bigalke et al., 2022; Järlskog et al., 2022; Kernchen et al., 2024).

In the context of MPs, TWPs, often referred to collectively as Tire and road wear particles (TRWP), are generated through the continuous friction between tires and the road surfaces, releasing particulates of different sizes, shapes and compositions that can be transported by wind or runoff (Kreider et al., 2010; Baensch-Baltruschat et al., 2020; Beji et al., 2023; Bondorf et al., 2025). TWPs constitute a complex mixture of diverse particulates (Gunawardana et al., 2012). Despite many studies already focused on the chemistry and morphology (Kreider et al., 2010; Sommer et al., 2018; Kim et al., 2021), eco-toxicology effects on human health (Wik et al., 2008; Marwood et al., 2011; Turner and Rice, 2010; Gualtieri et al., 2005), and overall emission

https://doi.org/10.5194/ar-2026-2
Preprint. Discussion started: 3 February 2026

AEROSOL Research Discussions

rates of these particles (Hillenbrand et al., 2005; Lee et al., 2019; Mennekes and Nowack, 2022), there remains a notable gap in understanding their behaviour pre and post deposition onto various surfaces, including road surfaces and other structures. Particularly, the mechanism by which these particles detach from, move across, and get entrained from these surfaces into the fluid flow remains understudied.

Similarly to dust and other MP particulate transport, multiple factors, including inherent entrainment forces such as aerodynamic drag and lift and stabilising forces such as adhesion, cohesion, electrostatic, and gravity, act at the interface between particles and the substrate, thus influencing the detachment behaviour of TWPs (Grigoratos and Martini, 2015; Esders et al., 2023). Existing studies on the aeolian dynamics and mechanisms governing MP detachment, resuspension and deposition under simulated free stream velocity and surface conditions have relied on using numerical models and experimental methods, which evolved from erosion modelling (Chepil, 1945; Shao and Li, 1999; Liu et al., 2019). Due to their simplicity and convenience, most experimental designs and models assume or sometimes prefer to use particles that are spherical in nature (Shao and Lu, 2000; Ibrahim et al., 2003). For instance, Esders et al. (2023) studied the effect of collision on the detachment behaviour of borosilicate and polyethylene (PE) particles of various sizes on glass substrate; they pointed out that collision plays a critical role in modulating the detachment threshold of these microspheres. The effect of surface roughness of substrates and particle sizes significantly influences the detachment threshold to mobilise and transport particles from surfaces, as studied by Kassab et al. (2013). On the contrary, perfect spherical particles are not the most common in environmental settings (Olivares et al., 2024), and the balance of forces could further be complicated by the irregular nature of particles which do not conform to the spherical assumptions. Interestingly, Olivares et al. (2024) performed experimental studies using irregular and flat-shaped micro particles, corroborated with a Monte Carlo simulation model. Their results highlighted that while smaller irregular particles may exhibit higher removal efficiency, the overall removal fraction of irregularly shaped particles remains significantly lower than that of glass microspheres of similar cohorts subjected to identical aerodynamic forces.

Understanding the importance of the u_*^{th} value is critical in particle detachment, as it represents the minimum wind-induced stress required to overcome adhesive and gravitational forces and initiate particle migration. Shao and Lu (2000) provided a theoretical force balance model for predicting u_*^{th}, originally formulated for spherical particles. They explicitly account for how cohesive forces such as van der Waals and electrostatic forces can dominate for smaller particles, while gravitational forces become more significant for larger ones. By balancing these forces against the aerodynamic forces, the particle type u_*^{th} can be predicted. Despite this model being validated primarily on spherical particles with experimental observations, it remains a core force balance framework which can be adopted for non-spherical particles (Del Bello et al., 2021). However, for particles such as TWPs associated with non-spherical geometries, it is important to validate some experimental results with the theoretical model in predicting the particle u_*^{th} of different sizes and shapes.

Compounding the complexity of particle detachment is the role of spatial deposition patterns. As implied, particle deposition is the process by which particles in suspension gravitationally settle onto surfaces. Various seeding approaches have been used in dust and powder depositional studies, including dust cloud producer (Goossens and Van Kerschaever, 1999), injection and fan mixing (Jiang et al., 2011), and some advanced pressurised solutions (e.g. the PALAS RBG 1000; Theron et al., 2020), to achieve a uniform, near monolayer deposit with minimal agglomerates. While some conventional seeding techniques, such

https://doi.org/10.5194/ar-2026-2
Preprint. Discussion started: 3 February 2026

as tipping and sieving, have also been used due to their low cost and simplicity (Qasem et al., 2011; Beattie et al., 2012; Chanchangi et al., 2020), they often settle in clusters, thereby introducing bias in predicting the u_*^{th} needed to dislodge particles. Consequently, to address the inherent limitations of these conventional approaches, we implemented a cost-effective and efficient alternative that achieves near-monolayer deposition with reduced agglomeration while being uniformly distributed, offering a more realistic, yet controlled solution for particle deposition on test surfaces.

Most previous detachment studies have employed traditional image processing approach to detect and count particles frame by frame. For instance, Esders et al. (2022) applied an algorithm requiring color intensity thresholding to quantitatively determine the number of microspheres in each frame. Similarly, an optical microscope system coupled with image analysis software, which also employs binary thresholding and water segmentation, has been used to quantify detached microspheres (Barth et al., 2014). However, this approach can be more time-consuming, prone to operator bias, and may lack the precision required for accurately identifying individual particles with complex shapes (Marsh et al., 2018; Zhu et al., 2021). Consequently, accurately detecting and quantifying MPs can be challenging without the use of more complex image processing or costly optical systems. Recently, the application of deep learning to environmental pollution research has expanded considerably (Astorayme et al., 2024; Ayinde et al., 2024; Zailan et al., 2022; Zhao et al., 2024), with growing focus on detection, segmentation, and quantitative characterisation of particulate pollutants and plastic debris in microscopic images (Zeng et al., 2021; Chazhoor et al., 2022; Thammasanya et al., 2024; Liang et al., 2023; Jia et al., 2024).

Convolutional neural networks (CNNs) underpin many of these DL models, enabling them to learn hierarchical feature representations that excel at detecting and delineating objects against complex backgrounds (Benali Amjoud and Amrouch, 2020). The use of CNN backbones such as ResNet, MobileNet, AlexNet, DenseNet and SchuffleNet models performed relatively well in classifying plastic waste (Chazhoor et al., 2022). We here underscore the breakthrough of these models in discerning smaller particles in the form of MPs. Xu and Wang (2024) used UNET and Unet2plus to accurately segment MPs collected from an urban water, and was able to achieve segmentation accuracy of 91.45 % and 91.08 % for Unet and Unet2plus respectively. Strikingly, MP particles within the range of $1-10$ μm performed relatively well using an exposure time of 0.4 s and confidence level reaching an approximate of 85.47 % (Lim et al., 2024). Notably, 'You Only Look Once (Yolo)' architectures have gained widespread recognition for their speed, accuracy, and flexibility in both object detection and instance segmentation (Firdauz et al., 2023; Li et al., 2023; Xu et al., 2023). The latest generation, YoloV8, developed by Ultralytics and launched in January 2023, offers enhanced performance, making it well-suited for various image processing tasks. Previously, other YOLO version has been used for Image detection and segmentation task, however more features are been added to improve on the model framework, and thus make it better, as more versions emerged (Lee et al., 2019; Hu and Xu, 2022), which has also been utilised by comparing different variant for detecting and categorising MPs in the marine environment (Akkajit et al., 2024). While DL techniques have seen growing use in MP studies, their application to understanding the processes of atmospheric detachment and resuspension remains unexplored.

To address these limitations, we employ the state of the art DL based instance segmentation YoloV8nano (YoloV8n) to quantify the detachment dynamics of TWPs, including characterising and comparing the spatial deposition pattern for detachment potential, thereby bridging the existing gap and enhancing our understanding of how TWPs behave on near-real-world

https://doi.org/10.5194/ar-2026-2
Preprint. Discussion started: 3 February 2026

surfaces. In light of these scientific needs, our research aimed to advance the experimental analysis of TWP detachment with special focus on **tire wear particles (TWPs) generated on a laboratory test stand from a passenger car (PC) test tire**, which are treated as an idealised, well-characterised reference material for isolating fundamental detachment mechanisms. We introduced a low-cost seeding technique tailored to deposit particles more uniformly and then compared it to commonly used tipping and sieving methods, aiming to minimise agglomerates and achieving a reproducible spatial distribution of particles. We then employ the aforementioned (YoloV8n) model to detect, segment, and characterise each individual TWP collected from the three different methods, and subsequently use it on the sequence of high temporal resolution images captured during the wind tunnel runs. This study addresses the following research questions:

- Which seeding method best achieves a representative and uniform deposition of TWPs on glass substrates?
- How do evolving aerodynamic conditions impact the detachment rates of TWPs, in contrast with microspheres of the same group?
- Does particle shape significantly alter the threshold friction velocity required for detachment?

This study is the first to experimentally investigate the detachment of TWPs from surfaces in a laboratory wind tunnel, providing an idealised, controlled environment, and to utilise deep learning techniques to analyse particle behaviour in turbulent flows. Answering these questions is crucial for enhancing our understanding of MP and TWPs transport, particularly regarding their behaviour and migration from surface-bound deposits before entrainment into the air.

2 Methodology

Conventional image processing techniques have been widely adapted to detect imageries and analyse particle detachment under turbulent flow conditions in the wind tunnel. However, these approaches require extensive manual preprocessing to reduce noise and capture key features, which may introduce subjective choices and be time-consuming when applied frame by frame to high-frequency image series. To overcome these shortcomings, we propose an integrated methodology that leverages advanced computer vision techniques to resolve particle detachment, including controlled particle seeding and standardised image acquisition, optimised training and retrospectively synchronised airflow measurements (Fig. 1). Although this flow chart provides a visual representation of the workflow, subsequent sections will elaborate on the experimental approaches employed in this study.

2.1 Wind tunnel experimental setup and particle seeding systems

The experiments were conducted in an open-circuit boundary layer wind tunnel (Fig. 2), which was also used and described by Esders et al. (2023). The wind tunnel features a 54 cm × 27 cm cross-section and is 730 cm long. The inner walls of the wind tunnel are lined with polystyrene foam, and flow is controlled by a set of 12 fans of diameter 26.5 cm (RAB O TURBO 250, DALAP GmbH; Germany), supported by a stepless transformer (LSS 720-K, Thalheimer Transformatorenwerke

https://doi.org/10.5194/ar-2026-2
Preprint. Discussion started: 3 February 2026

AEROSOL Research Discussions

GmbH, Germany) controlled and adjusted by an automated robotic system, which enabled smooth, continuous and reproducible variation of the output voltage up to the maximum level. A honeycomb structure is positioned at the upstream side of the airflow before the contraction zone to ensure a laminar flow enters through the contraction zone and into the test section. A HEPA filter (EU2 classification, 10 μm pore size; Erwin Telle GmbH, Germany) is installed at the outlet of the wind tunnel to remove residual particles from the flow before discharge into the outdoor air.

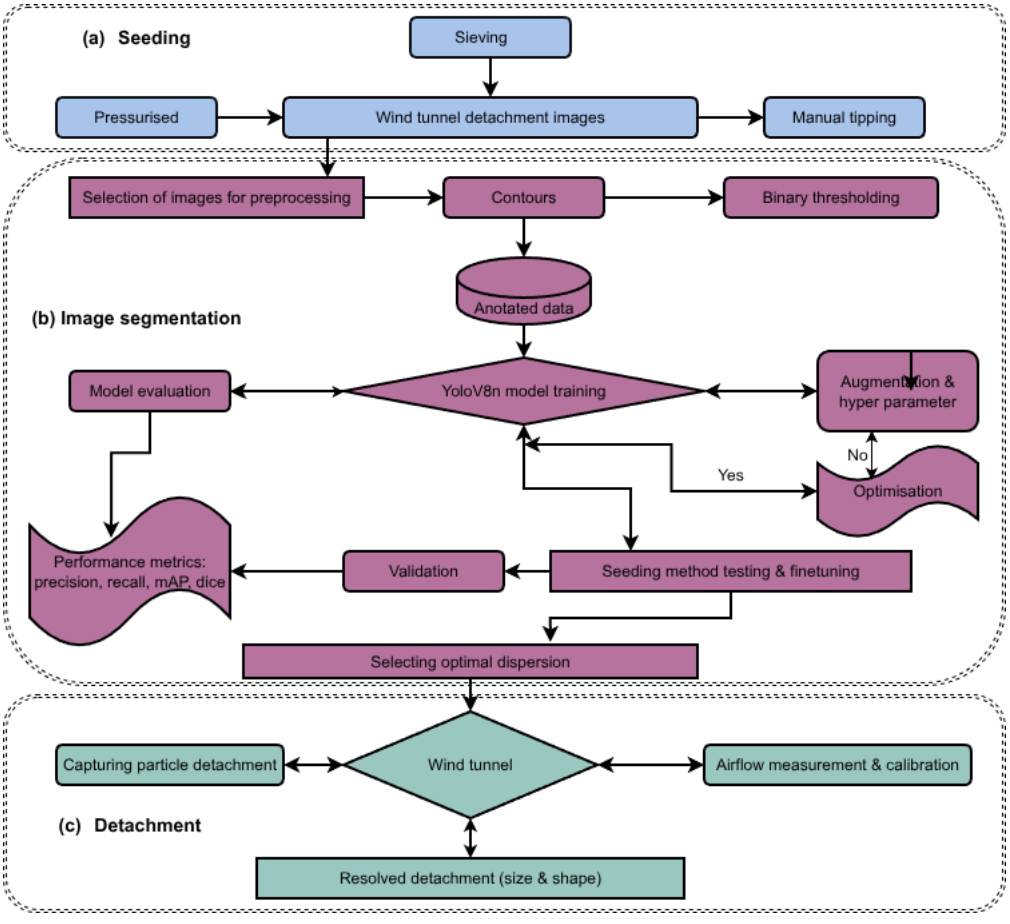

Figure 1. Overall structure of the experimental framework. This comprises three stages: (a) Seeding and high resolution image acquisition of particles via pressurised, sieving and tipping. (b) The deep learning based image segmentation and model optimisation. (c) Quantification of particle detachment and airflow measurement.

The test section is approximately 170 cm long and covered with an aerodynamically smooth lining at the bottom, onto which passive roughness elements in the form of LEGO® bricks are placed along the entire section of the test section to simulate the desired rough wall boundary conditions. To maintain a uniform surface consistency, a detachable substrate mount was positioned along the span of the roughness element such that the height of the mounted substrate was level with the height of the roughness element. A high-resolution camera (Sony Alpha 7RII) equipped with a long-distance microscopy lens (CF-1 lens,

https://doi.org/10.5194/ar-2026-2
Preprint. Discussion started: 3 February 2026

AEROSOL Research Discussions

K2 DistaMax Infinity, USA) was placed directly above the substrate mount with an adjustable object distance of approximately 35 cm to capture detachment events at 10 second interval, lighted by a 50W LED strip to illuminate the test section uniformly. Moreover, a three-dimensional hot-wire constant temperature anemometer (model 55P095, Dantec dynamics) mounted on a traverse system, is used to measure turbulent airflow statistics. A temperature probe for the CTA system (model 90P10, Dantec Dynamics) was also installed. In addition, a combined relative humidity sensor and temperature sensor (Model HC2A, Rotronic) was installed to record the air temperature and relative humidity (RH) of the system and compare them across runs.

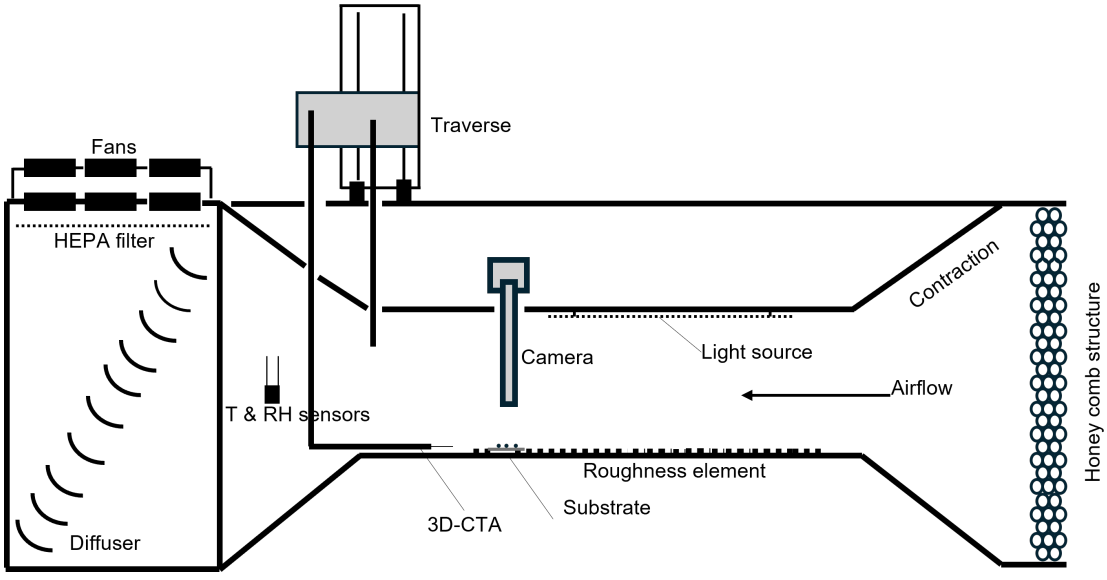

Figure 2. Diagram of the wind tunnel and test set up study the TWP detachment.

2.2 Tire wear particles and reference microspheres (PE115)

Pristine tire wear particles (TWPs) used in this study were generated on a laboratory test stand supplied by Continental GmbH. The material consists of tread-based compositions made from natural and synthetic rubber, with mineral fillers and standard additives, including components such as 6PPD and diphenylguanidine (DPG). The particles have not undergone road wear or environmental ageing and have not been mixed with road dust; therefore, they are treated as an idealised, well-characterised reference material. For the detachment experiments, TWPs from PC test tire were used. Additional TWPs from a truck-tire (TT) tire composition were used only to increase the diversity of particle morphologies in the image dataset for training and optimising the deep-learning framework. Representative high-resolution imagery of the PC TWPs (Fig. 3) was obtained using a scanning electron microscope (SEM). The TWPs exhibit irregular shapes and jagged textures with numerous sharp edges and span a broad range of sizes and aspect ratios.

As a spherical reference, polyethylene (PE) microspheres of comparable size cohorts were used, with a density of approximately $1025\ \mathrm{kg\ m^{-3}}$ (Esders et al., 2023). SEM images of the PE particles (see (Esders et al., 2023) show nearly perfectly spherical microspheres with smooth surfaces, in clear contrast to the irregular TWP aggregate. The density of the PC TWPs is

https://doi.org/10.5194/ar-2026-2
Preprint. Discussion started: 3 February 2026

about 1300 $\mathrm{kg\ m^{-3}}$, as specified by the manufacturer and consistent with values reported for comparable tire and tread wear particles (Klöckner et al., 2021).

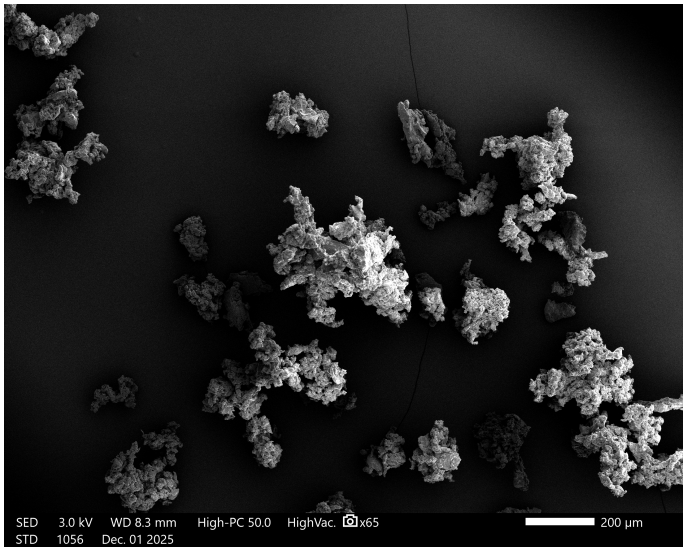

Figure 3. Scanning electronic microscopy imagery of passenger car tire wear particles.

2.3 Particle seeding methods and image acquisition

Prior to conducting the detachment experiments, three different particle seeding methods were evaluated for their ability to deposit particles homogeneously and as a monolayer onto the test substrate. These methods were assessed with the aim of minimising particle agglomeration, which can introduce significant bias in detachment measurements if not properly controlled (Kouadio et al., 2022). Some previous studies have used a simple cap tipping method for particle deposition. Among the few recent examples is the study by Esders et al. (2023), which employed this technique in MP detachment experiments using fluorescent microspheres. In their method, microspheres were stored in a sealed vial, which was flipped once to allow some particles to adhere to the inside of the cap. The cap was then unscrewed and gently tipped, allowing a small quantity of particles to fall gently onto the glass substrate (Fig. 4a). This method requires no specialised equipment beyond the vials and substrate, and its simplicity and gentle deposition makes it attractive for detachment studies. Despite some limitations, such as uneven particle distribution and low deposition throughput, we consider this method worth evaluating for our TWP seeding trials. Another easy and widely used approach in MP particle size fractionation and recovery is through sieving, which could be laboratory controlled and reproducible (Prume et al., 2021). Due to its reliability, we also adopted it for seeding the TWPs onto the substrates. Dried stacked stainless sieve with a mesh size of 200 μm (upper) and 150 μm (lower) were employed to isolate particles that are less than 200 μm onto the substrate (Fig. 4b). During the sieving process, gentle manual tapping was applied to the frame so that particles adhering to the mesh could easily dislodge, thereby reducing particle clusters.

https://doi.org/10.5194/ar-2026-2
Preprint. Discussion started: 3 February 2026

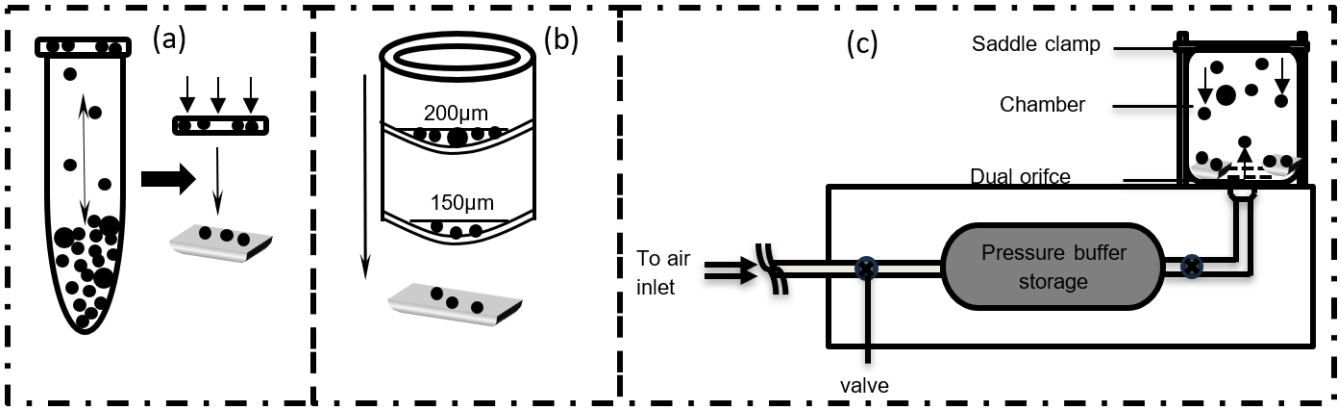

Figure 4. Diagram illustrating the three seeding methods. (a) cap tipping method (b) sieving method (c) developed low cost pressurised method

Due to the lumpiness of TWPs aggravated by their high rubber content, we developed a low cost pressurised seeding apparatus to reproducibly deposit a monolayer of particles while minimising the agglomeration on substrates (Fig. 4c). Particles are loaded onto a porous media filter housed in a custom, adjustable PVC socket and overlaid with a 600 μm sieve; together, these layers form a dual-orifice assembly that promotes uniform particle entrainment. Laboratory compressed air (6 bar) is regulated by a control valve and stored in a 2 L stainless steel pressure buffer (Festo CRVZS-2 HTI GmbH) fitted with a safety valve to cap the internal pressure at 2 bar. A solenoid valve (Bürkert type 0330) with a control switch then releases a short ($\sim$ 20 ms), high-velocity air pulse through the dual orifices into an airtight acrylic chamber secured by a saddle clamp. The substrates are placed inside the chamber so that particles ejected by the pulse of pressurised air gravitationally settle on them. This system also allows simultaneous seeding of multiple substrates in one operation, improving the throughput, reproducibility and efficiency. Finally, all three seeding methods were compared by placing the seeded substrates in the wind tunnel and capturing images at various orientations and replicate trials.

2.4 Background on deep learning YoloV8 Model

Yolo offers a range of models that are widely used for different computer vision tasks, including and not limited to object detection and instance segmentation (Redmon et al., 2016). This state-of-the-art model utilises CNN for feature extraction and originally used anchor boxes to detect objects of varying sizes and aspect ratios. However, since the model is built around a single-stage pipeline, it has a relatively higher processing speed compared to two-stage detections, such as Faster Region-based CNN (R-CNN). The input images are divided into grids that predict boundary boxes, confidence scores, and class probabilities. During the past few years, the Yolo architecture has undergone continuous refinements from YoloV3 and YoloV4 to YoloV5 and also to YoloV8, each iteration addressing limitations in speed, accuracy, and multi-task operations (Bochkovskiy et al., 2020; Jocher et al., 2023).

https://doi.org/10.5194/ar-2026-2
Preprint. Discussion started: 3 February 2026

Ultralytics released YoloV8 in January 2023, offering improved speed and accuracy compared to its predecessors. Its architecture comprises a backbone, a neck, and a head. In particular, it adopts a CSP-style that replaces the C3 block with the C2f module and uses a spatial pyramid pooling fast (SPPF) block for efficient multi-scale feature aggregation. Additionally, the detection head has been equipped with an anchor-free system, eliminating the manually configured anchor boxes, simplifying the model design, and improving its ability to detect objects of varying shapes and sizes. These improvements contribute to a better trade-off between the detection accuracy and processing speed, which is evident from the comparison of YoloV8 against its predecessors on the default 640px image resolution in Fig. A1, Appendix A, offering better throughput with similar number of parameters (Jocher et al., 2023; Hussain, 2023).

YoloV8 features different variants, ranging from nano (n) to extra large (x) models, providing diverse computational and performance requirements. On one hand, YoloV8n has fewer parameters and is optimised to deliver high inference speed with slightly lower accuracy as compared to the other variants. However, as the model progressively increases with depth from YoloV8s, YoloV8m, YoloV8l to YoloV8x, the accuracy increases while incurring more computational cost and higher inference speed, as evidenced by improved mAP scores in Fig. A1, Appendix A. Although larger models achieve superior detection performance, YoloV8n is highly efficient for real-time detection and frame-to-frame analysis, making it the preferred variant for our study.

2.5 Image segmentation

2.5.1 Data Preparation, Training and Optimization

To prepare the dataset for our YoloV8n instance segmentation model, we employed a semi automated annotation (SAA) workflow to efficiently generate accurate bounding box (BB) labels for densely populated TWPs. Manual creation of polygons around microparticles often exceeds 50 particles mm^{-2} and is both time-consuming and sometimes inaccurate. We therefore converted each image to grayscale and applied binary thresholding, selecting threshold values empirically based on image contrast to reliably separate particles from background noise. We then extracted contours from the binarized images, and then normalized each vertex's coordinates before converting into the Yolo instance segmentation format (see Fig. A2, Appendix A). We also enriched our training dataset by employing a grid based cropping strategy at equal vertical and horizontal strides producing eight sub images per original image, increasing sample diversity without altering particle appearance.

Table 1. Training and validation dataset (classes), before and after fine-tuning.

Phase	Label	Training Images	Validation Images
1	PC, TT	1158	802
2	TWP	562	204
3	TWP	1294	426

https://doi.org/10.5194/ar-2026-2
Preprint. Discussion started: 3 February 2026

The data were prepared in three phases, each split into training and validation sets (Table 1), to progressively refine the model's ability to segment micro-sized TWPs. Firstly, we trained the network on two classes PC and TT, which exhibit a wide range of particle sizes and shapes. Before training, we performed a grid search based hyperparameter optimisation (20 generations over the parameters in Table 2), monitoring training and validation loss convergence after 50 epochs to select the optimal configuration. The model was then trained for 1,000 epochs to establish baseline detection performance. Secondly, we fine-tuned the model on a new dataset with a smaller learning rate and reduced epochs, while we removed augmentations, and introduced multi scale image sizing to expose the network to scale diversity. Finally, the fine-tuned model was for a new set of data collected individually from the three seeding approaches.

For performing the model training and optimisation, we use a local workstation that runs on Ubuntu 20.04 LTS operating system equipped with an NVIDIA GeForce RTX 3090 GPU (8GB VRAM), an Intel Xeon W-2295 CPU (18 cores, 36 threads), and PyTorch 1.10 built with CUDA 11.2 and associated dependencies installed in python 3.10 environment. To supplement our local workstation and expedite model development, we also leveraged the TPU resources of Google Colaboratory (Colab), a free hosted Jupyter notebook environment used in parallel with our internal system to run additional training jobs. Despite using the Nano variant, model training remained computationally expensive. For a representative configuration with 960×960 image size, the Colab TPU setup processed roughly around 0.26 s per batch, whereas the local RTX 3090 processed around 1.2 s per batch, which is about 4 to 5 times slower, and this training execution time varies by the image size, number of epochs, and batch size. In contrast, the inference was relatively cheap, with minimal differences, and single-image processing took around 25 to 30 ms on Colab and 50 to 60 ms on the local workstation.

2.5.2 Performance Evaluation

To assess the generalisation capabilities of the model to detect and segment the BB and corresponding mask of the TWPs, we selected multi-faceted performance metrics to analyse the model, which encompass the precision, recall, and mean average precision (mAP) at different intersections over union (IoU) thresholds for both the BB and mask. The mAP evaluates the performance of segmenting the instances with value averaged, based on the IoU between the predicted and annotated ground truth (GT) BBs across the individual instances in the dataset. The IoU measure how well the predicted BB and mask fit with the annotated GT instance, defined by:

$$\text{IoU} = \frac{\text{Area of Overlap}}{\text{Area of Union}} \tag{1}$$

Where the numerator is the area of intersection between the pixels bounded by the annotated GT instances and predicted instances, while the denominator is the total pixels covered by the union of the GT and the predicted instances. On the other hand, precision measures the accuracy of positive predictions and recall evaluates the model's ability to identify relevant instances.

$$\text{Precision} = \frac{TP}{TP + FP} \tag{2}$$

https://doi.org/10.5194/ar-2026-2
Preprint. Discussion started: 3 February 2026

Table 2. Hyperparameters selected for the proposed model.

Parameter	Phase 1	Phase 2	Phase 3
Epochs	1000	200	50
Batch size	8	8	8
Initial learning rate	0.0001	0.00001	0.00001
Momentum	0.95	0.95	0.95
Weight decay	0.001	0.0005	0.0005
Image size	640	416, 640, 960, 1280	1280
Degrees	10	0	0
Scale	0.5	0	0
Translate	0	0	0
Mosaic	0.6	0	0
Hue factor	0	0	0
Saturation factor	0.5	0	0
Brightness factor	0.5	0	0
Horizontal flip	0	0	0
Vertical flip	0	0	0

$$\text{Recall} = \frac{TP}{TP + FN} \tag{3}$$

In the equation, FP, FN and TP are the total number of false positives, false negatives and true positives, respectively. To complement the other evaluation metrics, we also employed the Dice similarity coefficient (DSC) to individually discriminate TWPs that were segmented accurately. This DSC is a widely adopted metric to measure instance segmentation quality in medical and microscopy scale imaging, by penalising both FP and FN, providing a stricter measure of segmentation fidelity (Messer et al., 2024; Hajdowska et al., 2022). The DSC is defined as:

$$\text{DSC} = \frac{2|A \cap B|}{|A| + |B|} \tag{4}$$

where A represents the area of pixels in the predicted segmented mask, and B denotes the area of pixels in the binarised GT mask. The metric ranges from 0 (no overlap) to 1 (perfect overlap). By computing the DSC for each individual TWP, we were able to obtain a detailed evaluation of the model's ability to accurately delineate particle boundaries, quantifying the degree at which individual particles of different size and shape detach, and very efficient and sensitive to resolve TWPs capture on different surfaces.

https://doi.org/10.5194/ar-2026-2
Preprint. Discussion started: 3 February 2026

2.5.3 Sensitivity analysis

To investigate the robustness of the model and to establish reliable metrics for subsequent detachment studies, we investigated how sensitive the network's performance is to variations in the input image resolution. Yolov8n offers the lowest latency among the Yolov8 variants (see Fig. A1, Appendix A), which makes it well suited for frame by frame detachment tracking. However, the accuracy could be compromised at its default 640 px resolution. Therefore we fine tune the model at different input image resolutions specifically at 416, 640, 960 and 1280 px, holding other hyper-parameters constant, and comparing the resulting performance based on the evaluation metrics. This experiment quantifies the trade off between segmentation accuracy and computational speed, guiding the choice of the image size that preserves accuracy yet remains fast enough for the detachment analysis. Subsequently, we run an independent validation set with the three seeding methods based on the optimal image size, and then compute the particle attributes (equivalent diameter, circularity and corresponding DSC) for every segmented particle. This experiment enables a comparative evaluation of the seeding methods with respect to agglomerate reduction and size-dependent segmentation performance, thus providing the empirical basis for defining a DSC threshold and minimum particle size in resolving detachment.

2.5.4 Particle feature extraction

To evaluate the influence of particle morphology on detachment behaviour, we quantified two descriptors: equivalent diameter (D_e) and circularity (C). These features provide insights into the size and shape characteristics of the TWPs, which are critical factors affecting their adhesion and subsequent detachment from substrates (Ayinde et al., 2025). The D_e is particularly useful in characterising irregularly shaped particles, as it correlates with properties such as surface area and mass, which influence detachment behaviour (Kazemimanesh et al., 2022). The D_e is calculated as:

$$D_e = \sqrt{\frac{4A}{\pi}} \tag{5}$$

where A is the area of the particles expressed in pixels. On the other hand, the circularity which was first introduced by Cox (1927) as a shape factor, assessing how closely particle shapes approach that of a perfect sphere. It is computed using the formula:

$$C = \frac{4\pi A}{P^2} \tag{6}$$

Where P is the perimeter of the particle. The circularity value of 1 indicates a perfect sphere, while less than 1 denote increasing deviation from a sphere. In our study, the TWPs exhibit different shapes (see Fig. B1, Appendix B). This made this metric very instrumental in how elongated or irregularly the particles are, and how these exhibit different detachment behavior due to their variations in contact area and adhesion forces.

2.6 Parameter selection and optimisation

The trade-off between the performance and image input resolution for the deep learning model is evident, with detection accuracy improving consistently at higher resolutions (Fig. 5). The evaluated metrics precision, recall, mAP@50, and mAP@50-95

https://doi.org/10.5194/ar-2026-2
Preprint. Discussion started: 3 February 2026

AEROSOL Research Discussions

improve steadily with higher resolution for both the BB and the mask outputs, all based on 200 training epochs. The lowest resolution at 416 px produces the lowest precision and recall, with the highest missed detections and lowest confidence. As the image size increases to 640 px and 960 px, these metric improves, and at 1280 px, it achieves the maximum performance in precision and recall, indicating that the model detects more objects with greater confidence as the image size increases for both the BB and mask. In particular, the stricter metric (mAP@50-95) shows a notable jump at the largest resolution, especially for the mask prediction, reflecting more accurate localisation of objects. This suggests that finer object details and boundaries are being captured better with a higher input resolution. However, such behaviour is expected as altering the image size greatly affects the accuracy of any model, hence adapting a higher resolution image or images similar in resolution to those used during inference helps preserving more details and yield higher segmentation accuracy(Luke et al., 2019).

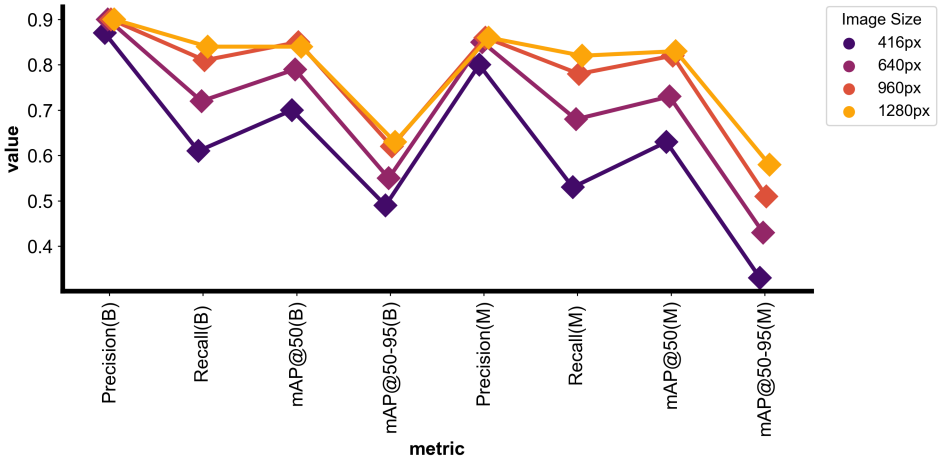

Figure 5. Sensitivity analysis of YoloV8 performance across input image resolutions. The figure evaluates the performance of YoloV8 for TWP detection at four input image sizes (416 px, 640 px, 960 px, and 1280 px). Metrics are shown for both bounding box (BB) and mask (M) predictions, evaluating how resolution impacts model accuracy in segmenting the TWP imagery.

Although the accuracy gains from higher resolution are compelling, they come with a significant trade-off in computational cost and training speed. Higher image resolution led to substantially longer training times compared to 416 px images, inevitably slowing down the detector. Conversely, this is consistent with Yolo model behaviour even across all the model variants, increasing in capacity, accuracy and computation as they progress with scales and sizing. In this case, the YOLOV8n variant was selected for its high throughput and efficiency, as mentioned in section 2.1, offering the best balance between speed and accuracy. Although larger variants such as YOLOV8s and YOLOV8m achieve slightly higher precision mAP@50 of 86.2 % and 87.6 %, respectively, compared to 83.6 % for YOLOv8n (Zhao et al., 2024), the improvement is modest relative to the more than two-fold increase in computational load. Therefore, the 1280 px input resolution was adopted, as it yielded the highest accuracy during training, while maintaining a fast inference rate suitable for frame to frame detachment analysis.

https://doi.org/10.5194/ar-2026-2
Preprint. Discussion started: 3 February 2026

AEROSOL Research Discussions

2.7 Comparative analysis of seeding methods

The three seeding methods employed to deposit TWPs onto the substrates yielded different particle distribution characteristics that influenced segmentation performance (Fig. 6). The tipping method produced the most heterogeneous distribution with pronounced agglomeration, resulting in a lower quality mask with most data points clustered at DSC $\leq$ 0.2 across most circularity and larger particles ($\geq 200\ \mu$m). Sieving demonstrated improved performance with reduced agglomeration, shifting the distribution of the DSC upward, particularly with particles with C < 0.6. The pressurised methods yielded the optimal dispersion, producing the clearest masks with large particles ($\geq 200\ \mu$m) consistently exceeding DSC 0.8, and even the smallest size category shows moderate segmentation accuracy. This seeding method disperses particles more uniformly across the substrate, reducing agglomerates as seen from the dense contour in Fig. 6c with smaller density exceeding the largest particle size category. Across all the methods, particle size and shape modulate segmentation accuracy. The larger the particle size, the more distinctive the edges and pixels are, so the DSC rises steadily with D_e. Conversely, smaller particles and those closer to a perfect sphere tend to give little textural details for the network to learn from, explaining why in Fig. 6c some small points remain near the least DSC.

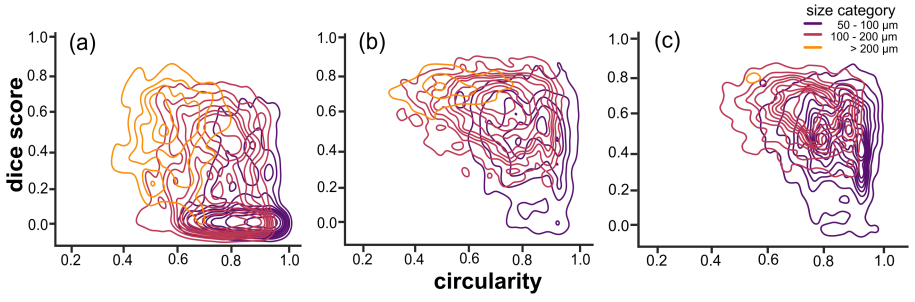

Figure 6. Comparison of particle segmentation accuracy across seeding methods. Plot showing relationship between shape, size and dice score where (a) is the tipping, (b) sieving and (c) pressurised method.

https://doi.org/10.5194/ar-2026-2
Preprint. Discussion started: 3 February 2026

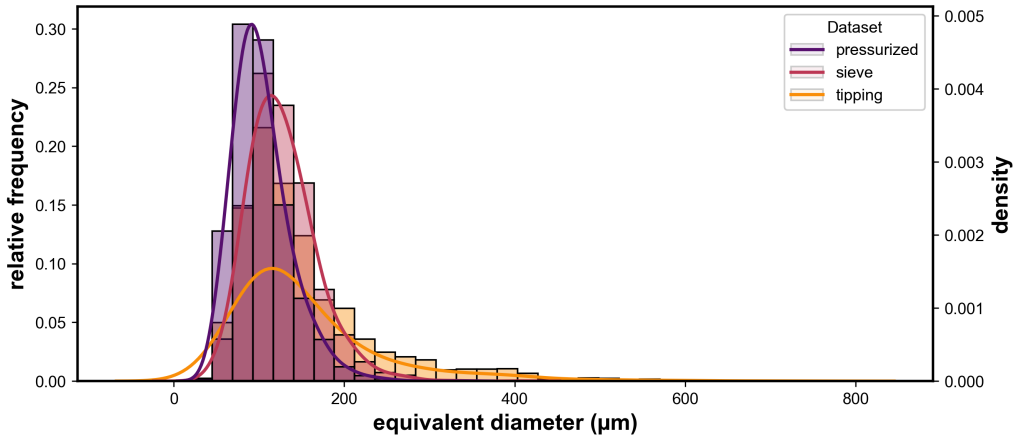

Figure 7. Distribution of TWPs by Seeding Method. This figure compares the particle size distribution (D_e) and deposition density of TWPs generated by three seeding methods: pressurised, sieve, and tipping. The relative frequency and density values reveal how each method influences particle uniformity and agglomeration on substrates.

The particle size distributions across the three seeding methods also reveal distinct uniformity and agglomeration behaviours, with all methods exhibiting unimodal rightly skewed patterns(Fig. 7). The pressurised method produces particles concentrated within the 80 - 180 μm range, with higher relative frequency and density at the peak, indicating a greater population which is evenly spread with optimised particle sizes. This distribution exhibits reduced right skewness, suggesting fewer oversized clusters. In contrast, the tipping method yielded a broader particle size distribution, characterised by higher right skewness and more frequent large clusters, reflecting increased agglomeration and spatial heterogeneity. Benchmarking against commercial equipment (Microtrac, Fig. B1, Appendix B), confirms that the pressurised method distribution aligns with the expectation from the laboratory analysis (125 – 200 μm), establishing optimal baseline to be used for future detachment studies.

2.8 Air flow characteristics

2.8.1 Velocity and turbulence measurement

To estimate the mean velocity and corresponding friction velocity (u_*), a logarithmic wind profile approach under the assumption of a neutral boundary layer (Hancock and Hayden, 2018) was employed to measure at different heights above the tunnel floor at 15 different heights using the CTA at a frequency of 10 kHz. The CTA provides measurement of the three-dimensional wind components: streamwise (u), cross-wise (v), and vertical (w) components were collected over 10 s intervals at each measurement point in the vertical profile under steady-state conditions, thus enabling the computation of turbulence statistics for detailed flow analysis. To assess reproducibility, four independent replicate measurements were performed for each wind speed stage. Prior to each wind tunnel run, the CTA was calibrated and automatically corrected for temperature variations to account for the small effect of temporal thermal variation, which could affect measurement precision. The mean wind speed profiles obtained were fitted to the logarithmic law of the wall (Foken and Mauder, 2008), where u_* was extrapolated using Eq. (7),

https://doi.org/10.5194/ar-2026-2
Preprint. Discussion started: 3 February 2026

and roughness length (z_0) computed accordingly. This approach verified the presence of a well developed boundary layer. In addition to the Prandtl method, the eddy covariance (EC) was utilised independently to estimate $u_{*,EC}$ at different heights. This was computed with other flow statistics using an automated software tool 'bmmflux' developed in the Micrometeorology group of University of Bayreuth for calculating atmospheric flow statistics (see appendix; Thomas et al., 2009).

$$u_{*,\mathrm{Pr}} = \kappa \cdot \frac{\partial \overline{U}}{\partial \ln(z)} \tag{7}$$

Where k is the von Karman constant (0.4). $u_{*,EC}$ values were compared with those obtained via $u_{*,Pr}$ to ensure consistency. To establish a direct relationship between the u_* computed by the two methods and surface velocity at the substrate position within the tunnel, a linear empirical equation was derived using ordinary least square regression. This ensured that the estimated u_* used in subsequent detachment experiments was unbiased and accurately reflected the aerodynamic conditions experienced in the system.

2.8.2 Friction velocity calibration

For modelling MP detachment, it is necessary to calibrate the u_* because it is the driving variable used at the surface to characterise detachment, which is always computed from extrapolating the vertical wind velocity at different heights using the log-law (Zhou et al., 2018). Hence, the u_* was calibrated in a similar fashion adapted in wall shear studies (Fernholz et al., 1996; Ibrahim et al., 2003; Zhang et al., 2024) by comparing two computational methods: one assumes the log-law of the wall across measurements at different distances from the wall, and the other one relies solely on the eddy-covariance (EC) momentum flux measured at a single height. Across the ten discrete stepwise stages used in this study, the free stream velocity (u_∞) ranges from 1.0 – 9.5 m s^{-1} for an average of four replicates conducted to achieve reproducibility. The logarithmic profile analysis returned u_* in the range of 0.098 – 0.798 m s^{-1} (see Fig. C1, appendix C), while EC yielded 0.066 – 0.769 m s^{-1} with around 3 % variation between the two methods. The z_0 intercepts at an average of 0.70 ± 0.1 mm, about 1/15 of the height of the roughness element at 10 mm, matching the 1/10 – 1/30 requirement reported for comparable geometric canopies (Fang and Sill, 1992). The longitudinal free stream turbulence intensity over the entire velocity range in the tunnel is $\leq$ 1 %. The comparison between these two methods confirms the test section achieves a fully developed turbulent flow (Fig. 8). The adjusted u_* was estimated from the regressed linear equation with an average uncertainty of $\pm 2\%$, accounting for CTA measurement errors and regression fitting uncertainties. The derived u_* calibration ($u_* = 0.174 \cdot \overline{U}(z)$) demonstrated strong agreement with independent methods, as the resulting u_* values deviated from direct log profile and EC measurements by only $\pm$ 4 % on average. This level of precision aligned with established wall shear methodologies (Dancey and Diplas, 2008) and confirmed the absence of systematic bias, validating its use for detachment analysis.

https://doi.org/10.5194/ar-2026-2
Preprint. Discussion started: 3 February 2026

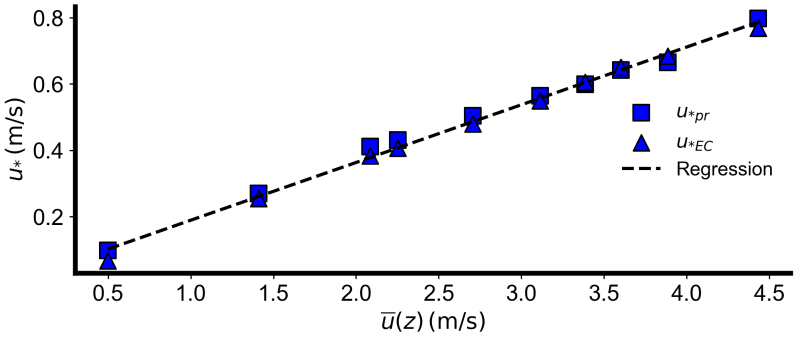

Figure 8. Calibration of u_* from the profile measurement and the EC against the surface wind velocity. $R^2 = 0.994$, and uncertainty for u_* is 0.010 m s^{-1} at 95 % CI.

2.9 Resolving particle detachment

2.9.1 Microplastics deposition and recording

Pristine TWPs were used as a proxy of irregularly shaped MPs to conduct the idealised detachment experiments (Sect. 2.2). The particles vary in size and shape (see Fig. B1, Appendix B), which are characterised using an optical particle analyser (Laser diffraction analyser, Microtrac Retsch GmbH) with sizes ranging predominantly from 125 μm to 200 μm. All particles were in pristine condition, with a material density of approximately 1300 kg m^{-3}. The detachment experiments were conducted on standard laboratory glass slides (Thermo Fisher Scientific), measuring 75 mm × 25 mm. Prior to testing, the glass slides were thoroughly cleaned following the protocol established by Ibrahim et al. (2003), ensuring the removal of surface impurities that could contribute to stabilising forces and interference with particle detachment.

Image acquisition for both training and detachment analysis was performed under identical conditions. The images and detachment events were controlled and monitored via computer tethering using the Sony Imaging edge desktop version 1.2.01.04031, which images were captured IN XAVC S HD format (1920 × 1080 pixels) at 10 s intervals. A clear image zoom was applied during acquisition, resulting in an effective field of view of approximately 18 × 12 mm. All images were stored frame by frame in a designated folder for subsequent analysis.

To ensure statistical reliability given the heterogeneity in particle size and shape, eight independent replicates were conducted under identical flow conditions. Particle seeding was achieved using our low-cost pressurised technique that enables an even distribution of TWPs across the glass surface. The average initial particle count was around 500 ± 250 particles / slide. Care was taken to prevent particle clustering. The particle laden substrates were mounted on a custom built holder aligned with the same level as the roughness elements. Seeding was performed immediately prior to each experiment to minimise exposure to environmental conditions that could influence particle adhesion. The particle-laden substrate was exposed to airflow applied in successive stages, each lasting 300 s, with the u_* incrementally increasing from 0 to 0.78 m s^{-1} over the course of the experiment. All experiments were conducted at ambient air temperatures of 18 ± 4° C and RH ranging from 21 % to 41 %.

https://doi.org/10.5194/ar-2026-2
Preprint. Discussion started: 3 February 2026

AEROSOL Research Discussions

2.9.2 Image treatment and particle detachment

The custom trained YoloV8n model (as discussed in section 2.5) in tandem with a customised Python script designed to automate object detection, mask extraction and detachment tracking was used to monitor and quantify particle detachment. It was applied frame by frame to identify and segment particles individually. Parameters such as projected area, perimeter BB dimensions, C and D_e are computed. A conversion factor of 9 μm / pixel was applied to translate the pixel based quantity into a physical metric in μm. Binary GT masks were created for all images to compute the DSC for the segmented particles individually. To ensure higher accuracy, only particles meeting the following criteria were retained: confidence level ≥ 0.1, DSC ≥ 0.5 (computed against the binary GT mask), $D_e \geq 30$ μm, and not touching the image boundaries.

To resolve the temporary changes and identify detached particles, a frame based tracking script was implemented, which assigned consistent particle IDs to particles detected in the first frame and matched them across subsequent frames using Euclidean distance between the BB centers. A distance threshold was used to determine whether the particle detached and moved or was still attached to the surface. Once the particle was no longer matched in subsequent frames, we considered it to be detached. All extracted data, including the particle ID, size and shape metrics, were saved in comma-separated format. The detachment fraction was computed as a fraction of particles no longer detected compared to the initial count. For each experiment, the detached fraction was defined as:

$$n_{det} = 1 - \frac{N(u_*, t)}{N_0} \tag{8}$$

where n_{det} is the fraction that detached with respect to u_*, $N(u_*, t)$ is the number of particles attached to the substrate at a certain incremental airflow exposure period, t, and N_0 is the initial particle number on the substrate. The detached fraction was normalised across the replicates and then binned into a fixed interval of 0.2. Within each bin, the mean friction velocity $\bar{u}_*$ and mean $\bar{n}_{\mathrm{det}}$ were computed. Subsequently, a two-parameter logistic function and an ordinary least square (OLS) regression model were fitted to the binned data.

$$N_*(u_*) = \frac{A}{1 + e^{-b(u_* - m)}} \tag{9}$$

$$\tilde{n}_{\mathrm{det}}(u_*) = a + b\,u_* \tag{10}$$

In the logistic case, A is the maximum detachment fraction, b is the rate of detachment change, and m is the inflexion point corresponding to the threshold fluid velocity u_*^{th}. The logistic function has been widely used to model resuspension response (Esders et al., 2023; Lim et al., 2025). Here, OLS regression was additionally fitted to test whether a simplified linear representation is sufficient to capture the observed detachment trends, and the goodness of fit was evaluated for both models using the coefficient of determination R^2.

To evaluate the influence of particle morphology on detachment behaviour, all detached particles were further stratified by D_e (80–150 μm, 150–300 μm) and C (0.3–0.6 μm, 0.6–0.8 μm, 0.8–1.0 μm). For each size and shape class, the normalised

https://doi.org/10.5194/ar-2026-2
Preprint. Discussion started: 3 February 2026

detachment data were recomputed, binned and fitted with both models as described above, and the corresponding u_*^{th} values (and their variability across replicates) were compared.

2.9.3 Predicting Threshold Friction Velocity

The theoretical framework developed by Shao and Lu (2000) is adopted to estimate the u_*^{th} based on a force balance acting on a stationary particle on a surface exposed to wind-induced shear stress. The model predicts the u_*^{th} required to initiate particle motion. This threshold condition is governed by particle properties, gravitational forces, and interparticle cohesion forces, and is expressed as:

$$u_{*th} = A_N \sqrt{\left(\sigma_p\, g d + \frac{\gamma}{\rho d}\right)} \tag{11}$$

where A_N is a dimensionless scaling parameter that controls how effective the applied shear surface shear stress is converted into aerodynamic forces acting on the particle, σ_p is the ratio of particle to air density, g is the gravitational acceleration, d is the particle diameter, γ is the interparticle cohesive force which ranges from 1.65 × 10-4 to 5 × 10-4 kg s^{-2} for dry particles. Although the Shao and Lu (2000) model has been extensively validated for monodisperse, spherical microspheres, its applicability to irregularly shaped particles such as TWPs with complex morphology remains unverified. TWPs experience more complex aerodynamic forces, but we hypothesise that their detachment can still be conceptually described within the force balance framework (Fig. 9). In this study, the microsphere data from Esders et al. (2022), obtained under comparable flow conditions, are treated as a reference case for which the Shao model and its parameter range have already been validated. We therefore do not recalibrate their dataset, but instead use it as a benchmark to evaluate how well the Shao framework agrees with the TWP detachment thresholds. To explore the sensitivity of the model, three calibration strategies are considered:

(i) Reference: A_N fixed at 0.111 and γ constrained to the original Shao and Lu range for dry particles

(ii) A_N fixed and γ allowed to vary within a wider plausible range to accommodate different effective cohesion of TWPs

(iii) both A_N and γ treated as free fit parameters, allowing the model to adapt more flexible to the estimated TWPs threshold.

We use these three options not to claim a unique parameter set for TWPs, but to illustrate how far the Shao and Lu framework can be modified and stretched to describe the TWP detachment threshold in relation to the established microsphere reference.

https://doi.org/10.5194/ar-2026-2
Preprint. Discussion started: 3 February 2026

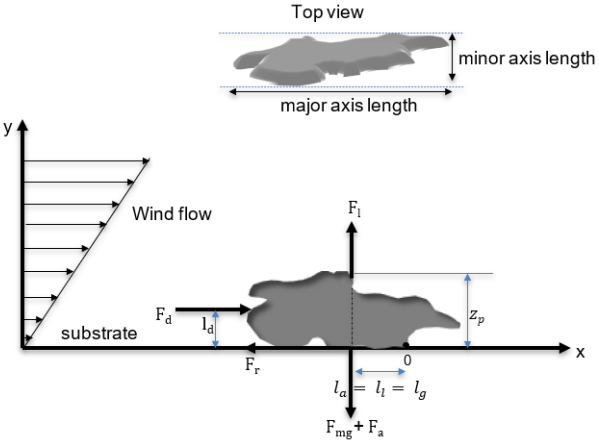

Figure 9. Forces acting on nonspherical particles on a surface, includes the aerodynamic; drag force (F_d), lift (F_l), stabilizing; adhesion force (F_a), gravitational force (F_{mg}), and frictional force (F_r), adapted from Olivares et al. (2024). When the moment of the aerodynamic forces exceeds the stabilising forces, the particle detaches and gets entrained into the flow.

3 Results and Discussion

This section presents three key findings from the idealised detachment experiments, which are quantification of TWP detachment as functions of particle morphology, comparison with the monodisperse microsphere as a benchmark, and finally evaluation of the performance of theorectical model against experimental threshold friction velocities.

3.1 Detachment experimental results

The experimental setup captured TWP detachment events across a 18 mm by 12 mm field of view on the glass surfaces, showing particles of different sizes and shapes (Fig. 10a). The deep learning framework detected over 90% of TWPs across image frames (Fig. 10b), demonstrating robust individual particle tracking with unique particle Identifiers. A DSC threshold of 0.5 validated segmentation masks, ensuring that the same particle was correctly tracked until it either detached from the glass surface or exited the camera frame. While MPs typically exhibit different detachment motions such as rolling, sliding and lifting on substrates before entrainment (Ibrahim et al., 2003; Kassab et al., 2013), our optical tracking focused explicitly on detachment events rather than distinguishing between motion modes. Some particles underwent small positional migrations before complete frame exit, requiring careful tracking to distinguish between temporary movement and actual detachment. In light of this, we employed a distance based particle matching technique using a threshold of 200 pixels, with equivalent to 1.8 mm to associate particles across frames. This defined distance ensured that particles maintaining their identification while migrating within the field of view were not prematurely classified as detached. A particle was only considered to be detached when it had moved beyond this matching threshold and could no longer be tracked across consecutive frames.

https://doi.org/10.5194/ar-2026-2
Preprint. Discussion started: 3 February 2026

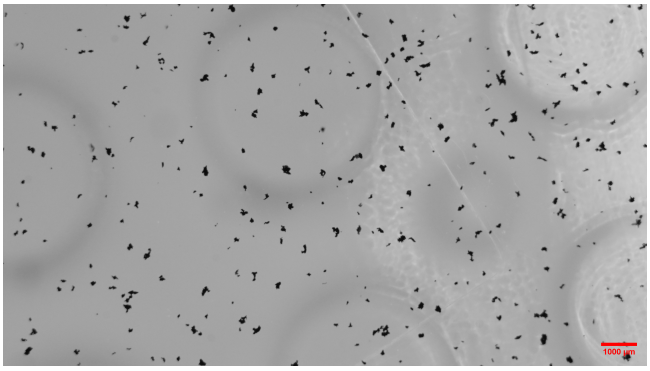

(a) Imagery of the TWPs deposited on the glass substrate, dispersed using the pressurised seeding method.

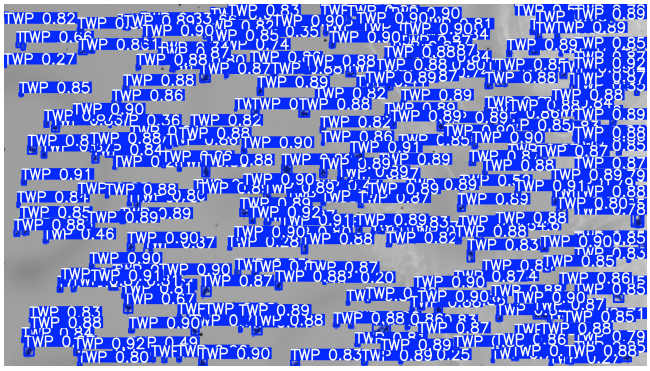

(b) Corresponding YOLOv8n inference results showing detected particles with bounding boxes and segmentation masks in blue (confidence threshold = 0.1).

Figure 10. Image pair illustrating the acquisition and DL based segmentation of TWPs on the glass test substrate.

The time evolution of the detachment fraction for all eight replicate experiments is shown as a function of time (Fig. D1, Appendix D). Notably, the detachments vary among the replicates. The remaining fraction on the substrate after the 30-min exposure time ranged from 57 % to 86 %. Such incomplete removal had been reported in detachment studies and depends on different factors, including exposure time and flow acceleration (Theron et al., 2020; Esders et al., 2022). In general, the TWPs were not detached at a single value of u_*, but over a range of incremented u_* values, with the cumulative detached fraction differing across replicates. During some detachment events, certain replicates exhibited a sharp initial jump in particle release immediately after the fan started. This behaviour is attributed to vibrations within the tunnel, which dislodge the weakest-bound particles first. Braaten et al. (1990) reported that particles with the smallest adhesion forces are removed first, whereas particles with larger adhesion forces require more turbulent flow or gusts occurring at random intervals to become detached. This observation is further supported by Ibrahim et al. (2003), who stated that lower adhesion moments during the acceleration phase lead to a higher net detachment rate compared to the steady state phase, where only random events generating drag and lift forces exceeded the average for removing MPs. Moreover, several factors such as air humidity may play a significant role. Kim et al. (2016) showed that resuspension rates fall sharply once the relative humidity exceeds 60 %. Our experiments were conducted at a moderate RH below 45 %, so detachment rate would likely be reduced under wetter conditions. Increased surface roughness also enhances the sheltering of particles. Kassab et al. (2013) reported less detachment on rough hardwood compared with glass. In contrast, since the glass substrate used in our study is smooth when looking at it on a macro scale, the sheltering effect is reduced, and hence adhesion could largely depend mainly on van der Waals forces and electrostatic forces (Zhang et al., 2025).

https://doi.org/10.5194/ar-2026-2
Preprint. Discussion started: 3 February 2026

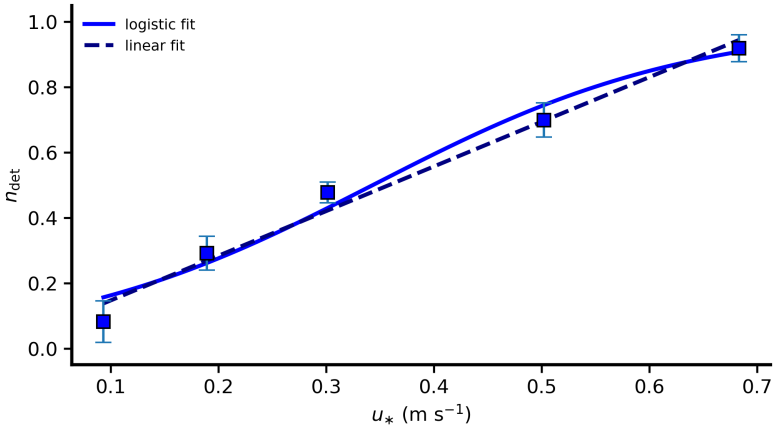

Figure 11. Normalised detached fraction of TWP as a function of friction velocity (u_*) for the eight replicates. The data points show ensembles averaged values (mean ± SD across samples). The solid line is the logistic fit ($R^2 = 0.97$); the dashed line is an ordinary least-squares linear fit ($R^2 = 0.98$).

Detachment rate spans a velocity range because adhesion is heterogeneous. Since detachment occurs across broad range of u_*, it is appropriate to define a representative u_*^{th} at which a significant fraction (50 %) of particles have detached (Ibrahim et al., 2003). The detachment curve shows a monotonic increase of the n_{det} with u_*, as described by the two models (Fig. 11). Applying both models to the ensemble binned data yielded very similar characteristic thresholds. The global logistic and OLS fit yield u_*^{th} of 0.34 m s^{-1} and 0.36 m s^{-1} respectively, and the mean u_*^{th} of the eight replicates was 0.36 ± 0.07 m s^{-1}. The spread across the binned points could be argued to indicate that TWPs experience broadly similar effective adhesion on the uniformly smooth glass substrate, suggesting that variability may be driven by differences in local contact geometry and microscale adhesion.

3.2 Investigating the effect of TWP size and shape on detachment rate

Particle morphology is another factor that influences detachment. Across all experiments, TWPs spanned a broad range of sizes and shapes (Fig.D2, appendix D), and the comparison of the initial and final population indicates that detachment does not occur uniformly across the distribution, but preferentially from a particular sub-range. D_e ranges from 80 μm $-$ 270 μm, with most particles between 100 μm $-$ 250 μm, and a peak between 120 μm $-$ 160 μm. C varies from 0.3 (highly irregular) to 1.0 (nearly spherical), with most particles clustering mainly between C of 0.6 $-$ 0.8, and only a few fractions being nearly spherical.

The u_*^{th} estimated from the detachment curves varied systematically with particle size (Fig. 12 A - C). For the smaller-sized bin (80 $-$ 150 μm), the mean u_*^{th} across samples was 0.45 ± 0.09 m s^{-1}, whereas the larger-sized bin (150 $-$ 300 μm) had a mean u_*^{th} of 0.58 ± 0.04 m s^{-1}. Thus, particles in the upper size bin detached at u_* roughly 25 % higher than those from the lower size bin, even though both belong to the same bulk population. This size dependence is consistent with findings from Del Bello et al. (2021), who reported lower thresholds for smaller (81 $-$ 89 μm) than for larger (110 $-$ 210 μm) irregular

https://doi.org/10.5194/ar-2026-2
Preprint. Discussion started: 3 February 2026

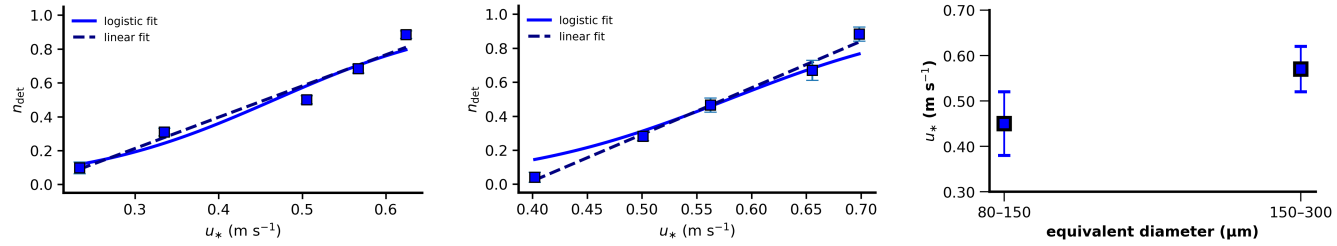

(a) $D_e = 80$–150 μm (b) $D_e = 150$–300 μm (c) Mean u_*^{th} as a function of size.

Figure 12. Size-resolved detachment behaviour of TWPs on the glass substrate. Panels (a) and (b) show the n_{det} as a function of u_* for the two D_e classes ($D_e = 80$–150 μm and 150–300 μm). Squares denote ensemble means ± 1 SD of the binned data; solid and dashed lines indicate the logistic and OLS fits, respectively. Panel (c) shows the mean u_*^{th} for the two size classes; error bars denote ± 1 SD across samples.

Particle shape quantified by C, also had a pronounced effect on detachment rate (Fig. 13 A - D). More rounded TWPs ($C = 0.8 - 1.0$) detached at substantially lower u_*^{th} values (0.46 ± 0.03 m s^{-1}), intermediate class ($C = 0.6 - 0.8$) at u_*^{th} values (0.51 ± 0.04 m s^{-1}), and the highly irregular TWPs ($C = 0.8 - 1.0$) at u_*^{th} values (0.58 ± 0.06 m s^{-1}). This monotonic increase in u_*^{th} with decreasing circularity shows that irregular TWPs are more resistant to aerodynamic removal than rounded ones. The underlying physical explanation is that irregularly shaped particles generally form stronger adhesive contacts with the surface due to increased contact area and multiple contact points. A highly irregular TWP can lie flat on the substrate with its deformable nature allowing it to maximise its contact area. By contrast, a spherical particle touches at a single point, minimising adhesive interaction. Although irregular particles may experience similar or even slightly enhanced aerodynamic forces due to extended parts reaching into higher velocity regions of the boundary layer, the effect is secondary to their substantially stronger adhesion. Consequently, the drag force (F_d) and lift force (F_l) can more easily pivot a more spherical particle off the surface, whereas an irregular particle having a lower centre of pressure and more contact points to the surface could be held back from detaching. In terms of the force balance schematic shown (Fig. 9), irregular particles possess a larger adhesion lever arm (l_a) because of their extended footprint, while simultaneously exhibiting a smaller drag lever arm (l_d) and a reduced area exposed to the airflow. Consequently, the aerodynamic moment $(F_d \, .l_d)$ is often insufficient to overcome the adhesion moment $(F_a \, .l_a)$, so a higher u_*^{th} is required for detachment.

https://doi.org/10.5194/ar-2026-2
Preprint. Discussion started: 3 February 2026

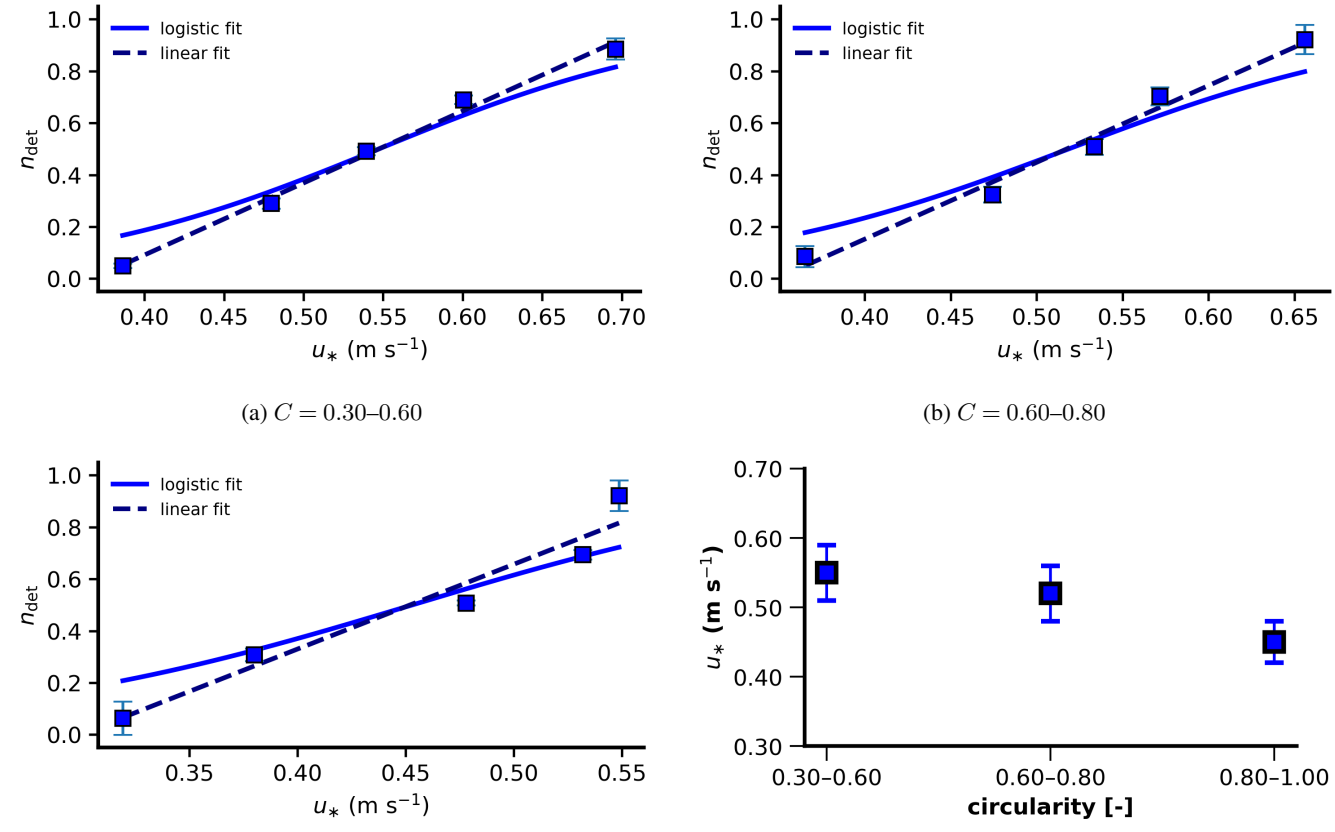

(a) $C = 0.30$–0.60

(b) $C = 0.60$–0.80

(c) $C = 0.80$–1.0

(d) Mean u_*^{th} as a function of shape.

Figure 13. Shape-resolved detachment behaviour of TWPs on glass substrate. Panels (a)-(c) show the n_{det} as a function of u_* for the three C classes ($C = 0.30$–0.60, 0.60–0.80, 0.80–1.00). Squares denote ensemble means ± 1 SD of the binned data; solid and dashed lines indicate the logistic and OLS fits, respectively. Panel (d) shows the mean u_*^{th} of the three shape classes; error bars denote ± 1 SD across samples.

These findings also align with other studies discussing particle shape effects. Olivares et al. (2024) reported that irregularly shaped particles showed significantly lower detachment rates compared to glass microspheres of the same cohort under similar conditions. Furthermore, Fig. 14 extends our comparison to PE microspheres of the same size cohort ($115\ \mu$m). In other words, under identical conditions, a PE microsphere might lift at half the shear force required to lift a comparable-sized TWP. This comparison can highlight how variability in particle morphology and particle roughness could alter the balance of forces. Thus, the elevated threshold observed for TWPs could arise due to the effect of a broad range of morphological differences.

3.3 Prediction of threshold friction velocity and comparison with microsphere

Across the investigated size range, the Shao and Lu fits reproduce the observed trend that TWPs require a higher u_*^{th} to initiate detachment compared to the PE microsphere (Fig. 14). For the PE microsphere reference data, the model with the standard empirical functions (see Eq. 11), returns γ to be 3.0×10^{-4} N m^{-1}, which lies comfortably within the range reported for

https://doi.org/10.5194/ar-2026-2
Preprint. Discussion started: 3 February 2026

AEROSOL Research Discussions

dry, loose dust and sand particles (Shao and Lu, 2000; Kok et al., 2012). This confirms that the reference parameterisation is appropriate for the PE microspheres. In contrast, applying the same parameter constraints to the TWPs clearly underestimates the measure thresholds. Even when γ is pushed to the upper limit of the empirical range 5.0×10^{-4} N m^{-1}, the predicted u_*^{th} curve remains below the observations, indicating that the unmodified Shao and Lu formulation does not fully capture the detachment behaviour of TWPs. Allowing γ to vary freely improves the fit, but the resulting value (3.0×10^{-3} N m^{-1}) is about 6 times the upper limit proposed for the natural dust and sand particles. Such a magnitude is difficult to reconcile with independent estimates of cohesive interparticle forces, including van der Waals forces for dry sediments and typical polymeric surfaces and would imply a strong cohesive contribution even in the size range where cohesion already dominates ($D_e < 75$ μm). Meanwhile, when both A_N and γ are treated as free parameters, the fitted curve recovers the expected increase in the u_*^{th} with particle size in the gravity-dominated regime. The best fit values (A_N = 0.34 and $\gamma = 1.0 \times 10^{-4}$ N m^{-1}), remain within the physically plausible bounds but require a substantially larger aerodynamic efficiency parameter. Similar variations in dimensionless threshold coefficients have been reported in aeolian studies, where analogous parameters (A_B, A_{ft}) vary with particle threshold Reynolds number (Re_{*t}), bed roughness, interparticle forces, and moisture effects (Iversen and White, 1982; Bagnold, 2012; Shao and Lu, 2000; Kok et al., 2012; Dong et al., 2007). In this context, the higher A_N for TWPs can be interpreted as an effective parameter that reflects morphological irregularity, multiple particle contact points with substrate, and micro-roughness.

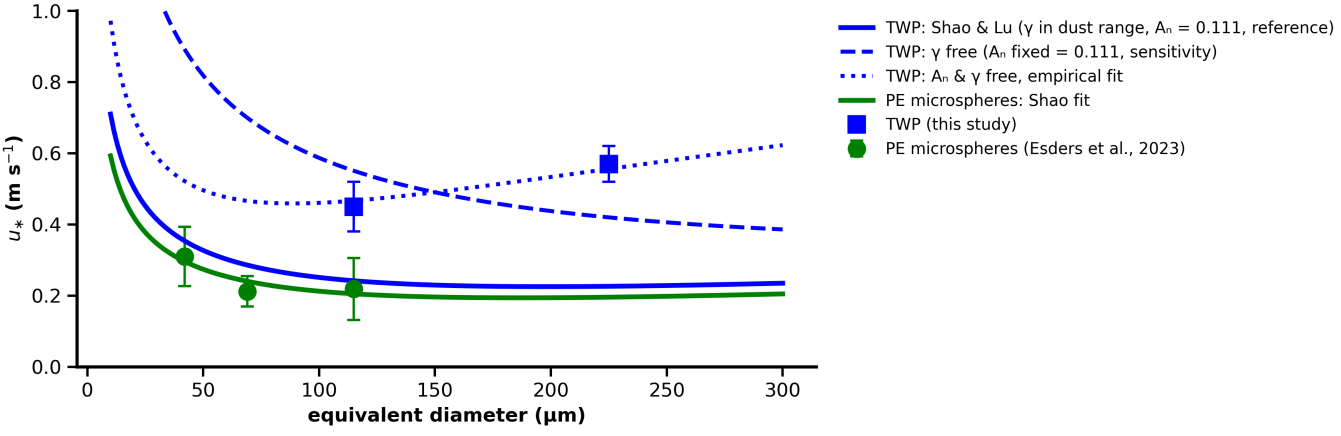

Figure 14. shows the u_*^{th} as a function of D_e for TWPs (blue squares), and PE microspheres (green circles; data from Esders et al. (2023)) on glass substrate. Error bars denote $\pm$ 1 SD). The solid blue line shows the Shao Lu model fit with dust parameter range, the dashed blue line shows a fit with A_N fixed and (γ) adjusted, and the dotted blue line shows the fit with both A_N fixed and (γ) adjusted. The solid green line is the Shao and Lu fit for the PE microsphere data.

Regardless of the calibration strategy, the TWP curve consistently lies above the PE microsphere curve. The density difference between TWPs and PE microspheres is too small to account for this offset alone. Within the Shao and Lu threshold framework, such a density contrast would influence the predicted u_*^{th} less than 10 %, whereas the measured thresholds differ

https://doi.org/10.5194/ar-2026-2
Preprint. Discussion started: 3 February 2026

by up to a factor of two. This observation aligns with previous studies (Del Bello et al., 2021; Olivares et al., 2024) which emphasise that particle geometry and roughness enhance the effective adhesion strength of irregularly shaped particles compared to smooth, spherical grains of similar size. Nevertheless, the role of density is not irrelevant, as it can also influence detachment thresholds, particularly for particles of similar morphology (Esders et al., 2023). Given the limited number of size bins available for the TWPs, the calibrated parameters should be regarded as exploratory, yet they reveal two robust findings from our idealised experiment: TWPs on smooth glass require considerably higher fluid thresholds than PE microspheres of comparable size, and the magnitude of this offset is best explained by enhanced effective cohesion and reduced aerodynamic leverage arising from TWP morphology rather than by density differences.

4 Conclusions

This study presents a quantitative framework to investigate the detachment behaviour of near-monolayer deposits of tire wear particles (TWPs) in the $80 - 300$ μm size range from an idealised glass substrate, by combining deep learning based image analysis with an optimised pressurised seeding technique for controlled particle deposition. Overall, our experiment shows that a bulk u_*^{th} of 0.36 m s^{-1} is required for TWP detachment, showing a clear increase with particle size and shape irregularity. Under similar surface shear, coarser and more angular TWPs tend to remain attached, while smaller and more rounded fragments are more readily mobilised, implying that surface stress preferentially entrains finer and more rounded TWPs rather than removing all deposited sizes and shapes uniformly. Comparison with PE microspheres of similar size corroborates this interpretation and demonstrates that density differences alone cannot account for the higher fluid thresholds observed; instead, particle morphology and strong surface adhesion emerge as the dominant controls on TWP detachment. These findings challenge the spherical particle assumptions embedded in widely used Shao and Lu empirical threshold models and highlight the need to explicitly account for morphology-informed parameterisation when representing TWPs and other irregularly shaped microplastics in resuspension schemes. While these results provide fundamental insights into TWP detachment behaviour, they are bounded by the studied size range and the idealised nature of pristine test stand TWPs on glass substrates. Hence, the work presented here should be regarded as a first, deliberately idealised step towards isolating key mechanisms controlling TWP detachment. Future studies should extend this framework to a broader particle size and density range, environmentally relevant tire wear and road particles (TWPs), and rough heterogeneous natural surfaces, and should include the role of mechanical perturbations to better capture behaviour under complex real-world conditions.

Data availability. Data supporting this study are available from the corresponding author upon reasonable request.

https://doi.org/10.5194/ar-2026-2
Preprint. Discussion started: 3 February 2026

AEROSOL Research Discussions

Appendix A

A1 Evolution of Yolo models

YoloV8n performance compared to other Yolo models and variants. The models were evaluated using the mAP^{50-95}_{val} metric on the MS COCO dataset (Jocher et al., 2023). YoloV8n performs better than the earlier nano variants but shows the lowest performance among the YoloV8 family. However, for detachment studies, a trade off between performance and inference speed is necessary.

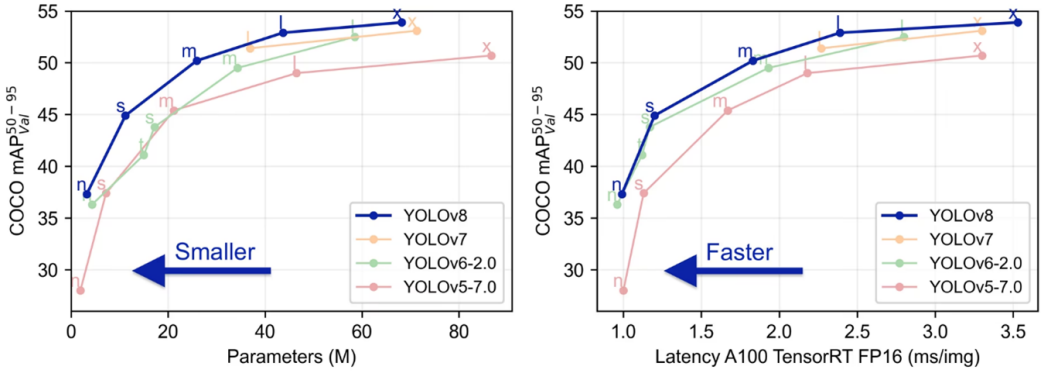

Figure A1. Comparison of the performance of YoloV8 with predecessors. Number of parameters (left), Inference speed (right)

.

A2 Preprocessing of YoloV8

The pipeline used for YoloV8 image annotation. This semi automated annotation approach was adopted instead of using the manual anonotation to extract the YoloV8 txt format labels, which were used for both the training and validation of the model.

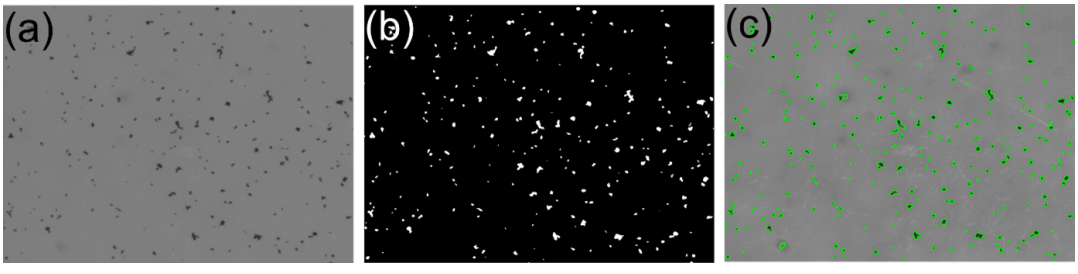

Figure A2. Preprocessing of YoloV8 Images (a) Sample of a raw image before preprocessing (b) Binary thresholding (c) contour outline.

https://doi.org/10.5194/ar-2026-2
Preprint. Discussion started: 3 February 2026

AEROSOL Research Discussions

A3 Performance evaluation

The mAP and loss curves obtained during training and validation on the TWP dataset, where the model weights corresponding to the best performance were selected.

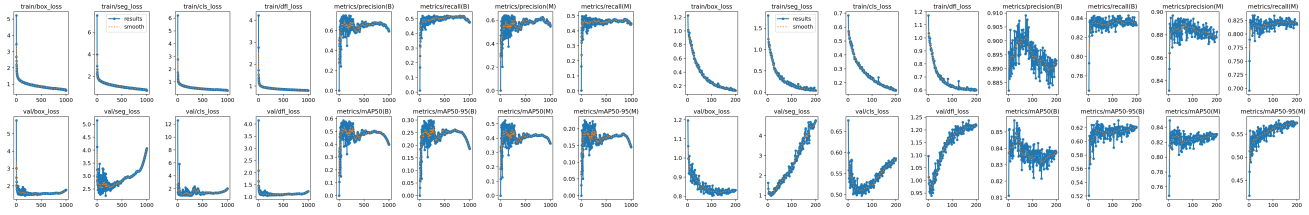

(a) metric evaluation for phase 1

(b) metric evaluation for phase 2

Figure A3. mAP and loss plots after training and validation on the TWP dataset

Appendix B

B1 Analytical analysis of the TWPs

The distribution of the TWP with different size and shape, analysed using the Microtrac analytical equipment. The datasheet was provided by department of macromolecular chemistry, University of Bayreuth.

https://doi.org/10.5194/ar-2026-2
Preprint. Discussion started: 3 February 2026

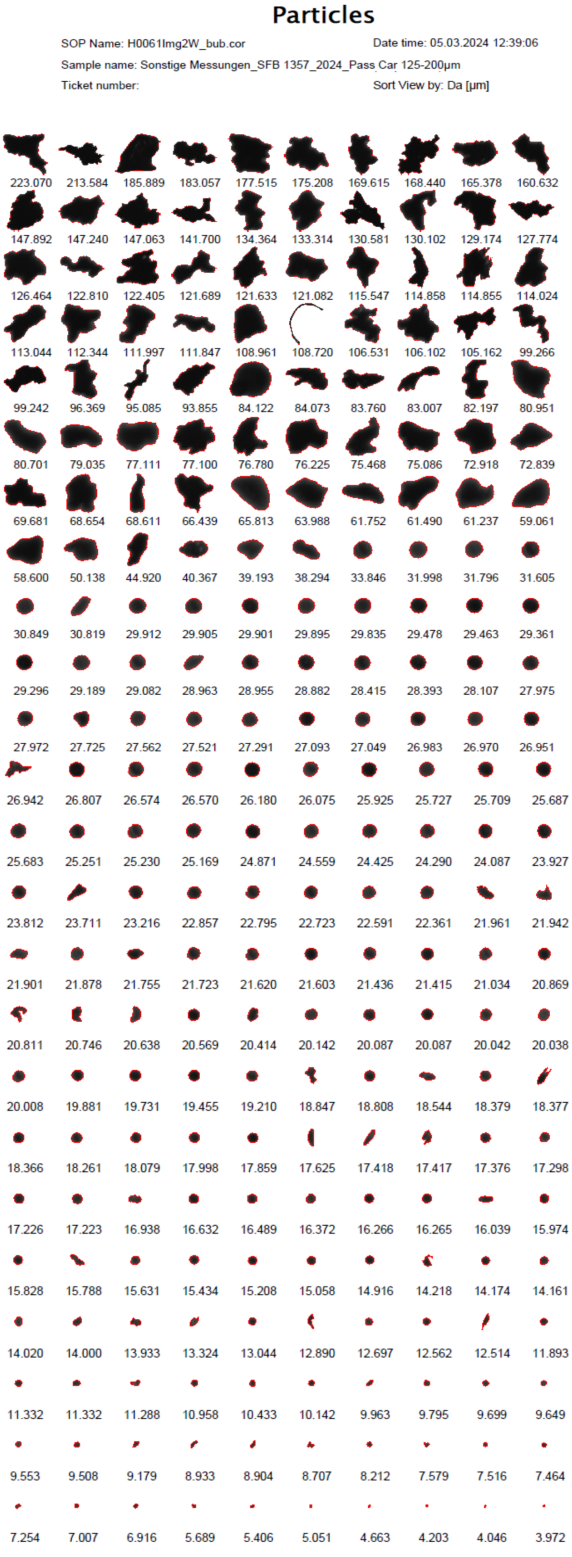

Figure B1. Size distribution of the PC TWPs.

https://doi.org/10.5194/ar-2026-2
Preprint. Discussion started: 3 February 2026

AEROSOL Research Discussions

Appendix C

C1 Flow conditions

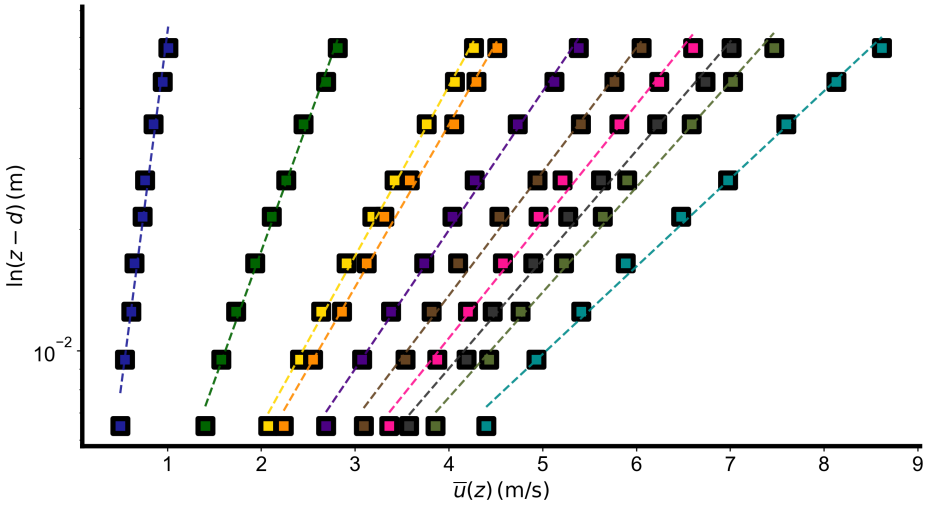

Figure C1. Logarithmic wind profile plots showing the relationship between the mean wind speed $\bar{u}(z)$ and logarithmic height $\ln(z-d)$ across the ten stages. Each color represents each stage, with the dashed lines indicating the linear fit to estimate the u_* and z_0 from the log wind profile equation with ($\kappa = 0.4$).

Appendix D

D1 Detachment

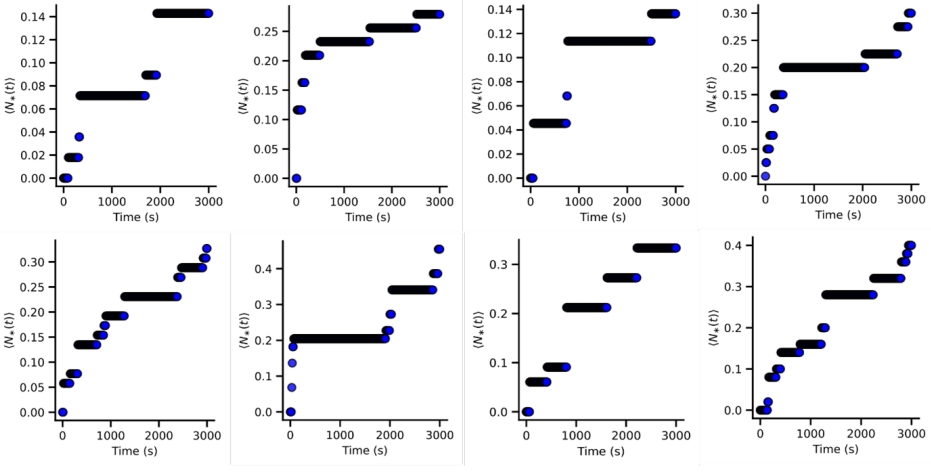

Figure D1. Detached TWPs for the eight replicates, showing the detachment fraction over the successive wind acceleration stages.

https://doi.org/10.5194/ar-2026-2
Preprint. Discussion started: 3 February 2026

AEROSOL Research Discussions

D2 Detachment

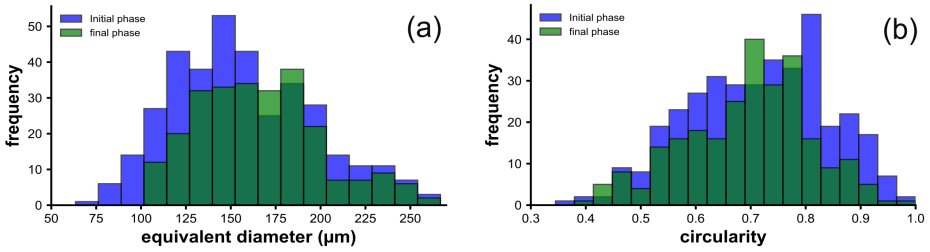

Figure D2. Comparison of particle morphology distribution at initial and final phase of detachment. (a) particle size distribution, larger particle size remained attached (b) circularity distribution, spherical particles were preferentially detached.

Author contributions. B.O.A conceived the project with C.K.T, conducted the wind tunnel experiments, designed the instrumental setup, analysed the data, and wrote the manuscript. J.O assisted with instrumental preparation with input from C.K.T and W.B. J.B and C.L provided material assistance. C.K.T, W.B, and A.N supervised the revision of the research and manuscript. D.W and S.A provided reference materials. All authors further read and commented on the paper.

Competing interests. There are no known competing interests.

Acknowledgements. We gratefully acknowledge financial support from the Deutsche Forschungsgemeinschaft (DFG, German Research Foundation) through the Collaborative Research Center (project numbers 391977956–SFB 1357 and 491183248). We thank Mathias Schott for his assistance with the scanning electron microscopic imaging of the passenger car tire wear particles (TWPs). We also thank Continental GmbH for their collaboration with the SFB Microplastics group and for providing the test stand-generated TWPs used in this study.

https://doi.org/10.5194/ar-2026-2
Preprint. Discussion started: 3 February 2026

References

Akkajit, P., Alahi, M. E. E., and Sukkuea, A.: Enhanced detection and classification of microplastics in marine environments using deep learning, Regional Studies in Marine Science, 80, 103 880, 2024.

Arthur, C., Baker, J., and Bamford, H.: Proceedings of the international research workshop on the occurrence, effects, and fate of microplastic marine debris, September 9-11, 2008, Tech. rep., 2009.

Astorayme, M. A., Vázquez-Rowe, I., and Kahhat, R.: The use of artificial intelligence algorithms to detect macroplastics in aquatic environments: A critical review, Science of The Total Environment, 945, 173 843, 2024.

Ayinde, B. O., Musa, M. R., and Ayinde, A.-A. O.: Application of machine learning models and landsat 8 data for estimating seasonal pm 2.5 concentrations, Environmental Analysis, Health and Toxicology, 39, e2024 011, 2024.

Ayinde, B. O., Babel, W., Olesch, J., Agarwal, S., Wagner, D., Nölscher, A., and Thomas, C.: Quantifying the detachment dynamics of microplastic car tire-wear particles using a deep learning framework in a laboratory wind tunnel., Tech. rep., Copernicus Meetings, 2025.

Baensch-Baltruschat, B., Kocher, B., Stock, F., and Reifferscheid, G.: Tyre and road wear particles (TRWP)-A review of generation, properties, emissions, human health risk, ecotoxicity, and fate in the environment, Science of the total Environment, 733, 137 823, 2020.

Bagnold, R. A.: The physics of blown sand and desert dunes, Courier Corporation, 2012.

Barth, T., Preuß, J., Müller, G., and Hampel, U.: Single particle resuspension experiments in turbulent channel flows, Journal of Aerosol Science, 71, 40–51, 2014.

Beattie, N. S., Moir, R. S., Chacko, C., Buffoni, G., Roberts, S. H., and Pearsall, N. M.: Understanding the effects of sand and dust accumulation on photovoltaic modules, Renewable Energy, 48, 448–452, 2012.

Beji, A., Deboudt, K., Muresan, B., Khardi, S., Flament, P., Fourmentin, M., and Lumiere, L.: Physical and chemical characteristics of particles emitted by a passenger vehicle at the tire-road contact, Chemosphere, 340, 139 874, 2023.

Benali Amjoud, A. and Amrouch, M.: Convolutional neural networks backbones for object detection, in: Image and Signal Processing: 9th International Conference, ICISP 2020, Marrakesh, Morocco, June 4–6, 2020, Proceedings 9, pp. 282–289, Springer, 2020.

Bigalke, M., Fieber, M., Foetisch, A., Reynes, J., and Tollan, P.: Microplastics in agricultural drainage water: a link between terrestrial and aquatic microplastic pollution, Science of the total environment, 806, 150 709, 2022.

Bochkovskiy, A., Wang, C.-Y., and Liao, H.-Y. M.: Yolov4: Optimal speed and accuracy of object detection, arXiv preprint arXiv:2004.10934, 2020.

Bondorf, L., Löber, M., Grein, T., Köhler, L., Epple, F., Schripp, T., Aigner, M., and Philipps, F.: Characterization of airborne tire particle emissions under realistic conditions on the chassis dynamometer, on the test track, and on the road, Aerosol Science and Technology, 59, 623–634, 2025.

Braaten, D., Shaw, R., et al.: Particle resuspension in a turbulent boundary layer-observed and modeled, Journal of Aerosol Science, 21, 613–628, 1990.

Cadle, S. and Williams, R.: Gas and particle emissions from automobile tires in laboratory and field studies, Journal of the Air Pollution Control Association, 28, 502–507, https://doi.org/https://doi.org/10.1080/00022470.1978.10470623, 1978.

Chanchangi, Y. N., Ghosh, A., Sundaram, S., and Mallick, T. K.: An analytical indoor experimental study on the effect of soiling on PV, focusing on dust properties and PV surface material, Solar Energy, 203, 46–68, 2020.

Chazhoor, A. A. P., Ho, E. S., Gao, B., and Woo, W. L.: Deep transfer learning benchmark for plastic waste classification, Intelligence & Robotics, 2, 1–19, 2022.

https://doi.org/10.5194/ar-2026-2
Preprint. Discussion started: 3 February 2026

Chepil, W.: Dynamics of wind erosion: I. Nature of movement of soil by wind, Soil Science, 60, 305–320, 1945.

Cox, E.: A method of assigning numerical and percentage values to the degree of roundness of sand grains, Journal of paleontology, 1, 179–183, 1927.

Dancey, C. L. and Diplas, P.: Statistical uncertainty and the estimation of log law parameters, Journal of Hydraulic Engineering, 134, 1353–1356, 2008.

Del Bello, E., Taddeucci, J., Merrison, J. P., Rasmussen, K. R., Andronico, D., Ricci, T., Scarlato, P., and Iversen, J. J.: Field-based measurements of volcanic ash resuspension by wind, Earth and Planetary Science Letters, 554, 116 684, 2021.

Dong, Z., Mu, Q., and Liu, X.: Defining the threshold wind velocity for moistened sediments, Journal of Geophysical Research: Solid Earth, 112, 2007.

Esders, E. M., Georgi, C., Babel, W., and Thomas, C.: Quantitative detection of aerial suspension of particles with a full-frame visual camera for atmospheric wind tunnel studies, Aerosol Science and Technology, 56, 530–544, 2022.

Esders, E. M., Sittl, S., Krammel, I., Babel, W., Papastavrou, G., and Thomas, C. K.: Is transport of microplastics different from mineral particles? Idealized wind tunnel studies on polyethylene microspheres, Atmospheric Chemistry and Physics, 23, 15 835–15 851, 2023.

Fang, C. and Sill, B.: Aerodynamic roughness length: correlation with roughness elements, Journal of Wind Engineering and Industrial Aerodynamics, 41, 449–460, 1992.

Fernholz, H., Janke, G., Schober, M., Wagner, P., and Warnack, D.: New developments and applications of skin-friction measuring techniques, Measurement Science and Technology, 7, 1396, 1996.

Firdauz, S. S., Rachmawati, E., and Sulistiyo, M. D.: Mask Detection on Motorcyclists Using YOLOv4, Building of Informatics, Technology and Science (BITS), 4, 2023.

Foken, T. and Mauder, M.: Micrometeorology, vol. 2, Springer, 2008.

Goossens, D. and Van Kerschaever, E.: Aeolian dust deposition on photovoltaic solar cells: the effects of wind velocity and airborne dust concentration on cell performance, Solar energy, 66, 277–289, 1999.

Gregory, M. R.: Plastic 'scrubbers' in hand cleansers: a further (and minor) source for marine pollution identified, Marine pollution bulletin, 32, 867–871, 1996.

Grigoratos, T. and Martini, G.: Brake wear particle emissions: a review, Environmental science and pollution research, 22, 2491–2504, 2015.

Gualtieri, M., Andrioletti, M., Mantecca, P., Vismara, C., and Camatini, M.: Impact of tire debris on in vitro and in vivo systems, Particle and fibre toxicology, 2, 1–14, 2005.

Gunawardana, C., Goonetilleke, A., Egodawatta, P., Dawes, L., and Kokot, S.: Source characterisation of road dust based on chemical and mineralogical composition, Chemosphere, 87, 163–170, 2012.

Hajdowska, K., Student, S., and Borys, D.: Graph based method for cell segmentation and detection in live-cell fluorescence microscope imaging, Biomedical Signal Processing and Control, 71, 103 071, 2022.

Hancock, P. E. and Hayden, P.: Wind-tunnel simulation of weakly and moderately stable atmospheric boundary layers, Boundary-layer meteorology, 168, 29–57, 2018.

Hillenbrand, T., Toussaint, D., Böhm, E., Fuchs, S., Scherer, U., Rudolphi, A., Hoffmann, M., Kreißig, J., and Kotz, C.: Einträge von Kupfer, Zink und Blei in Gewässer und Böden, 2005.

Horton, A. A. and Dixon, S. J.: Microplastics: An introduction to environmental transport processes, Wiley Interdisciplinary Reviews: Water, 5, e1268, 2018.

https://doi.org/10.5194/ar-2026-2
Preprint. Discussion started: 3 February 2026

Hu, Z. and Xu, C.: Detection of underwater plastic waste based on improved yolov5n, in: 2022 4th International Conference on Frontiers Technology of Information and Computer (ICFTIC), pp. 404–408, IEEE, 2022.

Hussain, M.: YOLO-v1 to YOLO-v8, the rise of YOLO and its complementary nature toward digital manufacturing and industrial defect detection, Machines, 11, 677, 2023.

Ibrahim, A., Dunn, P., and Brach, R.: Microparticle detachment from surfaces exposed to turbulent air flow: controlled experiments and modeling, Journal of aerosol science, 34, 765–782, 2003.

Iversen, J. D. and White, B. R.: Saltation threshold on earth, mars and venus, Sedimentology, 29, 111–119, 1982.

Järlskog, I., Jaramillo-Vogel, D., Rausch, J., Gustafsson, M., Strömvall, A.-M., and Andersson-Sköld, Y.: Concentrations of tire wear microplastics and other traffic-derived non-exhaust particles in the road environment, Environment international, 170, 107 618, 2022.

Jia, T., Peng, Z., Yu, J., Piaggio, A. L., Zhang, S., and de Kreuk, M. K.: Detecting the interaction between microparticles and biomass in biological wastewater treatment process with Deep Learning method, Science of the Total Environment, 951, 175 813, 2024.

Jiang, L., Fan, G., Li, Z., Kai, X., Zhang, D., Chen, Z., Humphries, S., Heness, G., and Yeung, W. Y.: An approach to the uniform dispersion of a high volume fraction of carbon nanotubes in aluminum powder, Carbon, 49, 1965–1971, 2011.

Jocher, G., Chaurasia, A., and Qiu, J.: YOLO by Ultralytics, 2023.

Kassab, A. S., Ugaz, V. M., King, M. D., and Hassan, Y. A.: High resolution study of micrometer particle detachment on different surfaces, Aerosol Science and Technology, 47, 351–360, 2013.

Kazemimanesh, M., Rahman, M. M., Duca, D., Johnson, T. J., Addad, A., Giannopoulos, G., Focsa, C., and Boies, A. M.: A comparative study on effective density, shape factor, and volatile mixing of non-spherical particles using tandem aerodynamic diameter, mobility diameter, and mass measurements, Journal of Aerosol Science, 161, 105 930, 2022.

Kernchen, S., Schmalz, H., Löder, M. G., Georgi, C., Einhorn, A., Greiner, A., Nölscher, A. C., Laforsch, C., and Held, A.: Atmospheric deposition studies of microplastics in Central Germany, Air Quality, Atmosphere & Health, 17, 2247–2261, 2024.

Kim, J., Yang, S. I., Moon, H., Hong, J., Hong, J., Choi, W., Son, H., Lee, B.-c., Kim, G.-B., and Kim, Y.: Potential release of nano-carbon black from tire-wear particles through the weathering effect, Journal of Industrial and Engineering Chemistry, 96, 322–329, 2021.

Kim, Y., Wellum, G., Mello, K., Strawhecker, K. E., Thoms, R., Giaya, A., and Wyslouzil, B. E.: Effects of relative humidity and particle and surface properties on particle resuspension rates, Aerosol Science and Technology, 50, 339–352, 2016.

Klöckner, P., Seiwert, B., Weyrauch, S., Escher, B. I., Reemtsma, T., and Wagner, S.: Comprehensive characterization of tire and road wear particles in highway tunnel road dust by use of size and density fractionation, Chemosphere, 279, 130 530, 2021.

Kok, J. F., Parteli, E. J., Michaels, T. I., and Karam, D. B.: The physics of wind-blown sand and dust, Reports on progress in Physics, 75, 106 901, 2012.

Kouadio, E. K., Goriaux, M., Laguionie, P., and Ruban, V.: Metal particle seeding on urban surface samples, Environmental Science and Pollution Research, 29, 30 837–30 849, 2022.

Kreider, M. L., Panko, J. M., McAtee, B. L., Sweet, L. I., and Finley, B. L.: Physical and chemical characterization of tire-related particles: Comparison of particles generated using different methodologies, Science of the Total Environment, 408, 652–659, 2010.

Laermanns, H., Lehmann, M., Klee, M., J. Löder, M. G., Gekle, S., and Bogner, C.: Tracing the horizontal transport of microplastics on rough surfaces, Microplastics and Nanoplastics, 1, 1–12, 2021.

Laforsch, C., Ramsperger, A. F., Mondellini, S., and Galloway, T. S.: Microplastics: a novel suite of environmental contaminants but present for decades, Regulatory toxicology, pp. 1185–1210, 2021.

https://doi.org/10.5194/ar-2026-2
Preprint. Discussion started: 3 February 2026

Laglbauer, B. J., Franco-Santos, R. M., Andreu-Cazenave, M., Brunelli, L., Papadatou, M., Palatinus, A., Grego, M., and Deprez, T.: Macrodebris and microplastics from beaches in Slovenia, Marine pollution bulletin, 89, 356–366, 2014.

Lee, Y., Lee, C., Lee, H.-J., and Kim, J.-S.: Fast detection of objects using a YOLOv3 network for a vending machine, in: 2019 IEEE International Conference on Artificial Intelligence Circuits and Systems (AICAS), pp. 132–136, IEEE, 2019.

Li, H., Yang, S., Zhang, R., Yu, P., Fu, Z., Wang, X., Kadoch, M., and Yang, Y.: Detection of floating objects on water surface using YOLOv5s in an edge computing environment, Water, 16, 86, 2023.

Liang, C., Jia, Z., and Chen, R.: An automated particle size analysis method for SEM images of powder coating particles, Coatings, 13, 1547, 2023.

Lim, J., Shin, G., and Shin, D.: Fast detection and classification of microplastics below 10 μm using CNN with Raman spectroscopy, Analytical Chemistry, 96, 6819–6825, 2024.

Lim, Y. K., Lee, C. H., Lee, K.-W., Hong, S. H., and Baek, S. H.: Impact of Heterosigma akashiwo on the environmental behavior of microplastics: Aggregation, sinking, and resuspension dynamics, Journal of Hazardous Materials, 487, 137 242, 2025.

Liu, Z., Zheng, C., Wu, Y., Flay, R. G., and Zhang, K.: Wind tunnel simulation of wind flows with the characteristics of thousand-meter high ABL, Building and Environment, 152, 74–86, 2019.

Luke, J., Joseph, R., and Balaji, M.: Impact of image size on accuracy and generalization of convolutional neural networks, Int. J. Res. Anal. Rev.(IJRAR), 6, 70–80, 2019.

Luo, Z., Zhou, X., Su, Y., Wang, H., Yu, R., Zhou, S., Xu, E. G., and Xing, B.: Environmental occurrence, fate, impact, and potential solution of tire microplastics: Similarities and differences with tire wear particles, Science of the Total Environment, 795, 148 902, 2021.

Marsh, B. P., Chada, N., Sanganna Gari, R. R., Sigdel, K. P., and King, G. M.: The Hessian blob algorithm: Precise particle detection in atomic force microscopy imagery, Scientific reports, 8, 978, 2018.

Marwood, C., McAtee, B., Kreider, M., Ogle, R. S., Finley, B., Sweet, L., and Panko, J.: Acute aquatic toxicity of tire and road wear particles to alga, daphnid, and fish, Ecotoxicology, 20, 2079–2089, 2011.

Mennekes, D. and Nowack, B.: Tire wear particle emissions: measurement data where are you?, Science of The Total Environment, 830, 154 655, 2022.

Messer, C., Khurana, R., and Bedi, S.: Classification of Uncertainty in Nuclei Segmentation From H&E Images, Tech. rep., 2024.

Olivares, M. V., Benito, J., Silin, N., Uñac, R., and Vidales, A.: Aerodynamic resuspension of irregular flat micro-particles, Journal of Aerosol Science, 181, 106 418, 2024.

Osuoha, J. O., Anyanwu, B. O., and Ejileugha, C.: Pharmaceuticals and personal care products as emerging contaminants: Need for combined treatment strategy, Journal of hazardous materials advances, 9, 100 206, 2023.

Piehl, S., Leibner, A., Löder, M. G., Dris, R., Bogner, C., and Laforsch, C.: Identification and quantification of macro-and microplastics on an agricultural farmland, Scientific reports, 8, 17 950, 2018.

Prume, J. A., Gorka, F., and Löder, M. G.: From sieve to microscope: an efficient technique for sample transfer in the process of microplastics' quantification, MethodsX, 8, 101 341, 2021.

Qasem, H., Betts, T. R., Mullejans, H., AlBusairi, H., and Gottschalg, R.: Effect of dust shading on photovoltaic modules, in: Effect of dust shading on photovoltaic modules, Loughborough University, 2011.

Redmon, J., Divvala, S., Girshick, R., and Farhadi, A.: You only look once: Unified, real-time object detection, in: Proceedings of the IEEE conference on computer vision and pattern recognition, pp. 779–788, 2016.

Shao, Y. and Li, A.: Numerical modelling of saltation in the atmospheric surface layer, Boundary-Layer Meteorology, 91, 199–225, 1999.

https://doi.org/10.5194/ar-2026-2
Preprint. Discussion started: 3 February 2026

Shao, Y. and Lu, H.: A simple expression for wind erosion threshold friction velocity, Journal of Geophysical Research: Atmospheres, 105, 22 437–22 443, 2000.

Sommer, F., Dietze, V., Baum, A., Sauer, J., Gilge, S., Maschowski, C., and Gieré, R.: Tire abrasion as a major source of microplastics in the environment, Aerosol and air quality research, 18, 2014–2028, 2018.

Sundt, P., Schulze, P.-E., and Syversen, F.: Sources of microplastic-pollution to the marine environment, Mepex for the Norwegian Environment Agency, 86, 20, 2014.

Thammasanya, T., Patiam, S., Rodcharoen, E., and Chotikarn, P.: A new approach to classifying polymer type of microplastics based on Faster-RCNN-FPN and spectroscopic imagery under ultraviolet light, Scientific reports, 14, 3529, 2024.

Theron, F., Debba, D., and Le Coq, L.: Local experimental methodology for the study of microparticles resuspension in ventilated duct during fan acceleration, Journal of Aerosol Science, 140, 105 477, 2020.

Thomas, C. K., Law, B. E., Irvine, J., Martin, J. G., Pettijohn, J. C., and Davis, K. J.: Seasonal hydrology explains interannual and seasonal variation in carbon and water exchange in a semiarid mature ponderosa pine forest in central Oregon, Journal of Geophysical Research: Biogeosciences, 114, 2009.

Turner, A. and Rice, L.: Toxicity of tire wear particle leachate to the marine macroalga, Ulva lactuca, Environmental Pollution, 158, 3650–3654, 2010.

van Calcar, C. v. and van Emmerik, T. v.: Abundance of plastic debris across European and Asian rivers, Environmental Research Letters, 14, 124 051, 2019.

Wik, A., Lycken, J., and Dave, G.: Sediment quality assessment of road runoff detention systems in Sweden and the potential contribution of tire wear, Water, air, and soil pollution, 194, 301–314, 2008.

Xu, J. and Wang, Z.: Efficient and accurate microplastics identification and segmentation in urban waters using convolutional neural networks, Science of The Total Environment, 911, 168 696, 2024.

Xu, S., Tang, H., Li, J., Wang, L., Zhang, X., and Gao, H.: A yolow algorithm of water-crossing object detection, Applied Sciences, 13, 8890, 2023.

Zailan, N. A., Azizan, M. M., Hasikin, K., Mohd Khairuddin, A. S., and Khairuddin, U.: An automated solid waste detection using the optimized YOLO model for riverine management, Frontiers in public health, 10, 907 280, 2022.

Zeng, T., Zhu, Y., and Lam, E. Y.: Deep learning for digital holography: a review, Optics express, 29, 40 572–40 593, 2021.

Zhang, P., Edwards, B. L., Webb, N. P., Trautz, A., Gillies, J. A., Ziegler, N. P., and Van Zee, J. W.: An evaluation of different approaches for estimating shear velocity in aeolian research studies, Aeolian Research, 70, 100 945, 2024.

Zhang, Z., Li, P., Hu, W., Li, J., Li, H., Wang, R., Li, Q., Zou, X., Zhou, B., Chang, C., et al.: Electric forces can enhance the emission of microplastics into air, Environmental Pollution, p. 126405, 2025.

Zhao, S., Zhou, H., and Yang, H.: Smart Monitoring Method for Land-Based Sources of Marine Outfalls Based on an Improved YOLOv8 Model, Water, 16, 3285, 2024.

Zhou, X., Zu, G., Gu, M., and Hu, J.: LES and wind tunnel test on friction velocity on roof surfaces, Cold Regions Science and Technology, 151, 109–118, 2018.

Zhu, Y., Yeung, C. H., and Lam, E. Y.: Microplastic pollution monitoring with holographic classification and deep learning, Journal of Physics: Photonics, 3, 024 013, 2021.